JGP Journal of General Physiology

ARTICLE

NMDA receptor channel gating control by the pre-M1 helix

Miranda J. McDaniel[1], Kevin K. Ogden[1], Steven A. Kell[1,2], Pieter B. Burger[2], Dennis C. Liotta[2], and Stephen F. Traynelis[1]

The NMDA receptor (NMDAR) is an ionotropic glutamate receptor formed from the tetrameric assembly of GluN1 and GluN2 subunits. Within the flexible linker between the agonist binding domain (ABD) and the M1 helix of the pore-forming transmembrane helical bundle lies a two-turn, extracellular pre-M1 helix positioned parallel to the plasma membrane and in van der Waals contact with the M3 helix thought to constitute the channel gate. The pre-M1 helix is tethered to the bilobed ABD, where agonist-induced conformational changes initiate activation. Additionally, it is a locus for de novo mutations associated with neurological disorders, is near other disease-associated de novo sites within the transmembrane domain, and is a structural determinant of subunit-selective modulators. To investigate the role of the pre-M1 helix in channel gating, we performed scanning mutagenesis across the GluN2A pre-M1 helix and recorded whole-cell macroscopic and single channel currents from HEK293 cell-attached patches. We identified two residues at which mutations perturb channel open probability, the mean open time, and the glutamate deactivation time course. We identified a subunit-specific network of aromatic amino acids located in and around the GluN2A pre-M1 helix to be important for gating. Based on these results, we are able to hypothesize about the role of the pre-M1 helix in other NMDAR subunits based on sequence and structure homology. Our results emphasize the role of the pre-M1 helix in channel gating, implicate the surrounding amino acid environment in this mechanism, and suggest unique subunit-specific contributions of pre-M1 helices to GluN1 and GluN2 gating.

Introduction

NMDA receptors (NMDARs) are a subfamily of ionotropic glutamate receptors whose calcium-permeable channels mediate the slow component of fast excitatory neurotransmission (Lester et al., 1990; Jahr and Stevens, 1993; Clements, 1996). These receptors, although necessary for synaptic plasticity, learning, and memory, have been implicated in the etiology of several neurological disorders, including epilepsy, intellectual disabilities, and schizophrenia (Coyle, 2006; Liu et al., 2004; Rice and DeLorenzo, 1998; Olney et al., 1999; Lemke et al., 2014; Traynelis et al., 2010; Yuan et al., 2015; XiangWei et al., 2018). NMDARs are formed from the tetramerization of two glycine-binding GluN1 subunits and two glutamate-binding GluN2 subunits. The GluN1 subunit is encoded by a single gene with eight possible splice variants. The GluN2 subunits, however, can be one of four discretely expressed gene products (A–D), each providing the receptor with unique pharmacological, physiological, and functional properties (Monyer et al., 1992; Cull-Candy et al., 2001; Traynelis et al., 2010; Paoletti et al., 2013).

Each subunit contains four semiautonomous domains: the amino terminal domain (ATD), the agonist binding domain (ABD), the transmembrane domain (TMD), and the carboxy-terminal domain. During a process referred to as gating, agonist binding to the ABD promotes channel opening within the TMD. Crystallographic data suggest that the bilobed ABDs initiate activation by adopting a closed-cleft conformation due to atomic contacts between the agonist, D1 upper lobe, and D2 lower lobe (Armstrong and Gouaux, 2000; Sun et al., 2002; Jin et al., 2003; Inanobe et al., 2005; Furukawa et al., 2005; Vance et al., 2011; Mayer, 2011; Karakas and Furukawa, 2014; Lee et al., 2014). Investigation of the α-amino-3-hydroxy-5-methyl-4-isoxazolepropionic acid (AMPA) receptor (AMPAR) by single molecule fluorescence resonance energy transfer has also contributed toward the understanding of site-specific transitions between multiple structurally distinct states. The ATD, for example, transitions between at least three distinct conformations in the desensitized state with interdimer distances ranging from 35 to 53 Å (MacLean et al., 2019). Moreover, single molecule fluorescence resonance energy transfer has been used to reveal conformational changes within the NMDAR transmembrane region associated with channel opening, which could account for the multiple receptor states observed in single channel recordings (Dolino et al., 2017). Gating of the AMPAR, a structurally

[1]Department of Pharmacology, Rollins Research Center, Emory University, Atlanta, GA; [2]Department of Chemistry, Emory University, Atlanta, GA.

Correspondence to Stephen F. Traynelis: strayne@emory.edu.

similar member of the ionotropic glutamate receptor family, involves a "kinking" of two nonadjacent, pore-forming M3 transmembrane helices away from the central axis of the pore (Twomey et al., 2017; Twomey and Sobolevsky, 2018). The AMPAR M3 helices contain a highly conserved amino acid sequence (SYTANLAAF), which can be found in all members of the ionotropic glutamate receptor family, including NMDARs. Finally, NMDARs exhibit similar asymmetry to that observed during AMPAR opening (Lee et al., 2014; Tajima et al., 2016), suggesting that this kinking motion also occurs for NMDARs.

Although the mechanism of NMDAR gating remains poorly understood, it has been hypothesized that the linker tethering the ABD to the TMD is responsible for facilitating communication between these two domains (Schorge et al., 2005; Sobolevsky et al., 2009; Talukder et al., 2010; Talukder and Wollmuth, 2011; Karakas and Furukawa, 2014; Lee et al., 2014; Gibb et al., 2018; Amin et al., 2020). Thus far, the flexible and dynamic nature of the ABD-TMD linker has prevented high resolution structure of this region, and the structure of the fully open NMDAR pore remains elusive (Tajima et al., 2016). Lower resolution analyses have revealed novel structural features within the linker that are uniquely positioned to transduce agonist binding into channel opening (Sobolevsky et al., 2009; Karakas and Furukawa, 2014; Lee et al., 2014).

Specifically, the linker between the ABD and the first transmembrane helix (M1) contains a short, two-turn pre-M1 helix that is thought to be a key contributor to the gating mechanism. The pre-M1 helix, previously described as a "cuff" helix, is hypothesized to participate in channel gating based on its orientation perpendicular to the channel pore, its position downstream of the ABD, and its van der Waals contact with the extracellular end of the M3 helical bundle (Sobolevsky et al., 2009; Karakas et al., 2015; Tajima et al., 2016). It stands to reason that agonist-induced closure of the bilobed ABD alters the position of the ABD-TMD linkers, leading to a reorientation of both the pre-M1 helices and the M3 helices of the GluN1 and GluN2 subunits (Sobolevsky et al., 2002; Furukawa and Gouaux, 2003; Furukawa et al., 2005; Inanobe et al., 2005; Vance et al., 2011; Hansen et al., 2013). In support of this hypothesis, it has been shown that cysteine substitutions within this linker region are sufficient to alter NMDAR responses, and MTS covalent modification of cysteine-substituted residues in this region altered receptor leak currents (Beck et al., 1999; Sobolevsky et al., 2007; Chang and Kuo, 2008). Therefore, if contact between the pre-M1 helix and the M3 helix is essential for stabilizing a closed channel state, then agonist-induced reorientation of the pre-M1 helix or its residue side chains may constitute a required, rate-limiting pregating step that must be traversed before the channel can open (Gibb et al., 2018).

The probable involvement of the pre-M1 helix in the gating mechanism is emphasized by human genetics. In a population of >140,000 healthy individuals (available from gnomad.broadinstitute.org), the GluN2A and GluN2B pre-M1 helices are devoid of missense variants, suggesting strong selection against variation in this region. By contrast, the pre-M1 helices of these subunits harbor multiple de novo mutations in patients with epilepsy, intellectual disabilities, or developmental delays (Swanger et al., 2016; Ogden et al., 2017; XiangWei et al., 2018; Amin et al., 2020). Within the GluN2A and GluN2B subunits, functional analysis of these disease-associated mutations revealed changes to NMDAR kinetics, further implicating the pre-M1 helix in the gating mechanism (Ogden et al., 2017; Gibb et al., 2018).

It has been proposed that the pre-M1 helix is one third of a triad also comprising the M3 pore-forming helix and the pre-M4 helix of the adjacent subunit (Chen et al., 2017; Ogden et al., 2017; Gibb et al., 2018). That is, two distinct triads exist in the tetrameric assembly: GluN1–pre-M1/GluN1-M3/GluN2–pre-M4 and GluN2–pre-M1/GluN2-M3/GluN1–pre-M4. As such, there might arise structural differences in each triad as a result of the different sequences for the GluN1 or GluN2 pre-M1 and pre-M4 helices. That is, global receptor asymmetry and disparate amino acid environments may contribute to subunit-specific pre-M1 contributions to the gating mechanism.

Functional data suggest that the GluN2A pre-M1 helix plays a larger role in gating than its GluN1 counterpart. Analysis of the GluN2A-P552R mutation showed a significant delay in receptor activation and deactivation, a finding that could not be recapitulated by the GluN1 equivalent mutation GluN1-P557R (Ogden et al., 2017). Additionally, data have shown that alanine mutations within the pre-M1 helix of the GluN2D subunit significantly alter receptor open probability (Ogden and Traynelis, 2013). Because open probability is a property of the NMDAR that differs greatly between GluN2A/2B and GluN2C/2D, we might expect that residues within the pre-M1 helix, specifically those that differ between the two groups, might account for these differences. As such, we explored the GluN2A pre-M1 helix for its role in gating to better understand both its mechanistic function and how this differs from that of the pre-M1 helix in other subunits. We conducted site-directed mutagenesis coupled with two-electrode voltage clamp, single channel, and whole-cell patch clamp recordings to directly monitor changes in receptor pharmacology, response time course, and microscopic properties. We also ran MD simulations of the receptor in the presence of agonist to investigate atomic interactions between the pre-M1 helix and surrounding residues. Our results identified GluN2A-F553 as a significant contributor to receptor gating and suggest that local intra- and inter-subunit amino acid side chain interactions may be important for subunit-specific pre-M1 contributions to this mechanism.

Materials and methods

Molecular biology

cDNAs for recombinant rat NMDAR subunits GluN1-1a (hereafter GluN1; GenBank accession no. U08261 for GluN1 lacking exon 5 but containing exons 21 and 22) and GluN2A (GenBank accession no. D13211) were subcloned into a mammalian expression vector (pcIneo). We introduced point mutations into the GluN2A cDNA using Quikchange reactions (Agilent Technologies). For expression in *Xenopus laevis* oocytes, DNA constructs were linearized by restriction enzymes and used as templates for in vitro cRNA transcription using the mMessage mMachine kit (Ambion) according to the manufacturer's recommended protocol.

Two-electrode voltage clamp recordings from *Xenopus* oocytes

Defolliculated stage V-VI *Xenopus* oocytes were obtained from EcoCyte Bioscience or oocytes in ovaries were obtained from *Xenopus* 1, and individual oocytes were defolliculated and injected with GluN1 and GluN2A cRNA at a 1:2 ratio (5–10 ng total in 50 nl water), as previously described (Hansen et al., 2013; Ogden and Traynelis, 2013). Following injection, oocytes were maintained for 2–7 d at 15°C in Barth's culture medium containing 88 mM NaCl, 2.4 mM $NaHCO_3$, 1 mM KCl, 0.33 mM $Ca(NO_3)_2$, 0.41 mM $CaCl_2$, 0.82 mM $MgSO_4$, and 5 mM HEPES (pH 7.4) and supplemented with 0.1 mg/ml gentamicin sulfate and 1 µg/ml streptomycin. Oocytes were placed in a recording chamber and continuously perfused with a solution containing 90 mM NaCl, 1 mM KCl, 10 mM HEPES, 0.5–1 mM $BaCl_2$, and 0.01 mM EDTA (pH 7.4). Responses were measured at room temperature (21–23°C) for 0.10–100 µM glutamate in 100 µM glycine, and 0.03–30 µM glycine in 100 µM glutamate. Microelectrodes were fabricated from borosilicate glass (TW150F-4; World Precision Instruments), filled with 0.3–3 M KCl, and currents were recorded under two-electrode voltage clamp at a holding potential of −40 mV (OC-725C; Warner Instruments). Currents were low pass filtered at 10 Hz and digitized at 20 Hz using custom acquisition software (EasyOocyte). Additionally, channel open probability was calculated from the degree of MTS ethylammonium (MTSEA) potentiation. Currents were evoked by 100 µM glutamate and glycine. In the continued presence of agonists, 200 µM MTSEA was applied and the degree of potentiation was determined. The following equation was used to determine open probability (P_{Open}) as a function of potentiation:

$$P_{Open} = (\gamma_{MTSEA}/\gamma_{Control}) \times (1/Potentiation)$$

Potentiation is the current after MTSEA treatment divided by the current before treatment. The control and MTSEA chord conductance γ were estimated from GluN1/GluN2A receptors (Yuan et al., 2005).

Whole-cell current recordings from transfected HEK293 cells

HEK293 cells (ATCC CRL-1573) were plated onto glass coverslips coated with poly-D-lysine (100 µg/ml) and transiently transfected using the calcium phosphate precipitation method (Chen and Okayama, 1987) with plasmid cDNAs encoding GluN1, WT, or mutant GluN2A, and GFP at a ratio of 1:1:1 (0.2 mg/ml total cDNA). 200 µM D,L-APV and 200 µM 7-chlorokynuernic acid were added to the tissue culture media to reduce activation of the NMDARs by ambient glutamate, thereby reducing excitotoxic cell death. Cells were transferred to a recording chamber 18–24 h after transfection and continuously perfused at 2 ml/min with solution containing 150 mM NaCl, 3 mM KCl, 10 mM HEPES, 0.01 mM EDTA, 0.5 mM $CaCl_2$, and 11 D-mannitol (pH 7.4). Patch electrodes were made from thin-walled filamented borosilicate glass (catalog no. TW150F-4; World Precision Instruments) pulled using a Flaming/Brown horizontal puller (P-1000; Sutter Instrument) and fire polished to a final resistance of 3–4 MΩ. The pipettes were filled with a filtered solution composed of 110 mM D-gluconic acid, 110 mM CsOH, 30 mM CsCl, 5 mM HEPES, 4 mM NaCl, 0.5 mM $CaCl_2$, 2 mM $MgCl_2$, 5 mM BAPTA, 2 mM Na-ATP, and 0.3 mM Na-GTP (pH 7.35). The osmolality was 300–310 mOsmol/kg. The membrane potential of HEK293 cells was held at −60 mV using an Axopatch 200B patch-clamp amplifier (Molecular Devices). NMDAR current responses were recorded during application of 1 mM glutamate and 30 µM glycine at room temperature (23°C). Current recordings were filtered at 8 kHz (−3 dB, 8 pole Bessel filter) and digitized at 20 kHz using a Digidata 1440A data acquisition system (Molecular Devices) controlled by Clampex 10.3 (Molecular Devices). The rise time for each response was determined as the time measured between 10% and 90% of the peak current. The current response time courses were averaged in Clampfit 10.6 (Molecular Devices), and the deactivation time course was fitted using ChanneLab by the sum of two exponential functions:

$$Current(time) = Amp_{Fast}\, e^{(-time/\tau_{Fast})} + Amp_{Slow}\, e^{(-time/\tau_{Slow})},$$

where τ_{Fast} is the fast deactivation time constant, τ_{Slow} is the slow deactivation time constant, Amp_{Fast} is the amplitude of the fast deactivation component, Amp_{Slow} is the amplitude of the slow deactivation component, and the peak response at the initiation of deactivation occurs at time = 0. Weighted deactivation time constants (τ_w) were determined by the following equation:

$$\tau_w = \{[Amp_{Fast}/(Amp_{Fast} + Amp_{Slow})] \times \tau_{Fast}\} + \{[Amp_{Slow}/(Amp_{Fast} + Amp_{Slow})] \times \tau_{Slow}\}$$

Single channel recordings from transfected HEK293 cells

Cell-attached patch recordings were made at room temperature (23°C) from HEK293 cells transiently transfected with rat GluN1, GluN2, and GFP, as described above. The extracellular recording solution was the same as in whole-cell recordings, except the pH was adjusted to 8.0. Micropipettes were made using thin-walled glass as for whole-cell recordings, coated with Sylgard silicone elastomer (Dow), and fire polished to a resistance of 4–6 MΩ. Patch pipettes were filled with recording solution supplemented with 1 mM glutamate and 50 µM glycine. The holding potential was +80 mV for cell-attached patches, which corresponded to a membrane potential of approximately −100 to −120 mV, as zero current was observed at −20 to −40 mV and the reversal potential for NMDARs is 0 mV. Currents were low pass filtered at 8 kHz (−3 dB, 8-pole Bessel) and digitized at 40 kHz. Patches were determined to contain a single channel when no double openings were observed and analysis of opening frequency suggested a low probability ($P < 0.001$) of a multichannel recording (Colquhoun and Hawkes, 1990). Single channel records were analyzed off-line using QUB software (Qin et al., 1996; Qin et al., 1997). The critical time (T_{crit}) used to chop the idealized dwells into bursts was determined as previously described (Jackson et al., 1983; Magleby and Pallotta, 1983). Individual open and closed dwell times were determined using a dead time of 0.05 ms and fitted with the sum of multiple exponential components using the maximum likelihood method. All values reported are mean ± SEM.

Homology modeling and MD

A human GluN1/GluN2A dihetero-tetrameric homology model was constructed from a glutamate/glycine-bound, exon

5–lacking GluN1a/GluN2B crystal structure (Protein Data Bank [PDB] identifier, 4PE5; 3.96 Å resolution; Karakas and Furukawa 2014), an exon 5–containing GluN1b/GluN2B crystal structure in the nonactive conformation (PDB identifier, 5FXH; 5 Å resolution; Tajima et al., 2016), and the TMD of the GluA2 crystal structure (PDB identifier, 5L1B; 4.0 Å resolution; Yelshanskaya et al., 2016). The alignment of the target and template sequences was performed using multiple sequence comparison by log-expectation (Edgar, 2004). Five homology models were generated using Modeller v9.19 (Sali and Blundell, 1993) from which the lowest energy model was selected and subjected to quality analysis using the PDBsum generator (Laskowski et al., 2018). The selected model structure is provided in Table S1. Hydrogen bond assignments were performed, followed by subsequent optimization and visual inspection. All titratable residues were assigned their dominant protonation state at pH 7.0 (Schrödinger Release 2018–4; Protein Preparation Wizard; Epik version 3.7; Impact version 7.2; Prime version 4.5, 2017; Schrödinger, LLC). Energy minimization was performed to relieve unfavorable interactions. The minimization process first involved minimizing only hydrogen atoms, followed by a restrained minimization using the imperf tool with a convergence of the RMSD of heavy atoms to 0.3 Å. Using a separate copy of this WT model, GluN2A-Phe553 was mutated to alanine for use in a second MD simulation (Schrödinger Release 2019–1, Schrödinger Suite 2019–1 Protein Preparation Wizard; Epik, 2016; Impact, 2016; Prime, 2019; Schrödinger, LLC).

To accelerate the MD simulations, each structure was truncated to exclude the ATD (residues removed up to residue 393 for the GluN1 subunits and up to residue 424 for the GluN2A subunits; Fig. 1; the structure is provided in Table S1). For both the WT and GluN2A-F553A model, the optimized and truncated receptor was inserted into an equilibrated palmitoyl oleoyl phosphatidyl choline bilayer. Membrane placement was assigned manually using the Orientations of Proteins in Membranes database (Lomize et al., 2012) entry for the 4PE5 template as a visual guide, ensuring charged residues at the intracellular end of the TMD fell outside of the hydrophobic section of the membrane. Solvation of the protein structure was done using the simple point charge water model; the solvation box included a 10-Å buffer between the protein and periodic boundary. The overall WT (F553A values in parentheses) system was neutralized by the addition of 10 Na^+ ions, with the NaCl concentration set to 150 mM. The system, consisting of 1,696 amino acids, 391 (391) lipid molecules, 47,571 (47,559) waters (simple point charge), and 132 (132) NaCl atoms, totaling 222,177 (222,121) atoms with a box size of 129 × 120 × 140 Å (2,167,200 $Å^3$; same dimensions for both the WT and GluN2A-F553A systems) was treated using the OPLS3e force field within the Desmond module of the Schrödinger software package (Desmond Molecular Dynamics System, D. E. Shaw Research). Following the Desmond membrane protein relaxation protocol, two independent 250-ns production runs—one for each receptor (WT and GluN2A-F553A)—were performed at a constant temperature of 310°K and pressure of 1.013 bar with particle mesh Ewald electrostatics using a cutoff of 9 Å for each system. Time-step calculations were performed every 2 fs, and frames were captured every 100 ps. Analysis of the MD trajectory was performed in Desmond and visual MD (VMD; Humphrey et al., 1996). RMSD analysis of the simulations is presented in Fig. S1 (the resulting trajectories are available from Burger and Kell, 2020). A discrepancy is present between the model residue numbering and that of the sequence numbering in the original trajectory files. We have provided a key and useful Python commands at the end of Table S1 to help with renumbering. Additional files with instructions on how to renumber the residues, as well as a TCL script for use in VMD, are also available at the link provided above.

For each of the two trajectories, frames were extracted from the 250-ns simulation at 200-ps intervals. These frames were clustered using the "cluster" function within VMD, an implementation of the quality threshold algorithm (Heyer et al., 1999), with an RMSD-based distance function. PDB files for the frames closest to the center of the largest cluster for each trajectory, which were used in Fig. 6, B–D, are provided in Table S1; the residues in these files are correctly numbered and do not require renumbering. The residues considered for clustering for each simulation include only those shown in Fig. 6, B and D. Additional details and analysis of the model and MD runs are provided in Figs. S2., S3., S4., S5., and S6.

Statistical analysis

Statistical analysis was conducted using OriginPro 9 or GraphPad Prism 7. Measurements are given as mean ± SEM, with the exception of the concentrations of agonist that produces a half-maximal response (EC_{50}), which are reported as mean with the 95% confidence intervals determined from the log (EC_{50}). For glutamate and glycine potency, no overlap in confidence intervals was considered significant. For the deactivation time course, data were analyzed using one-way ANOVA with Tukey's post hoc test. Significance was set at $P < 0.05$ compared with WT, and the number of observations was selected to give power >0.95 for a minimum detectable difference of 50% for weighted τ. When multiple parameters were compared from the same recording (e.g., Fig. 3), we corrected for familywise error.

Online supplemental material

RMSD analysis of the MD simulations is presented in Fig. S1. Fig. S2 provides distributions of distances between pairs of aromatic residues across each of the MD simulations as shown in Fig. 6. Fig. S3 and Fig. S4 show the sequence alignments used for homology model building, along with the sequence identity and similarity between the templates and the target. Ramachandran plots and structure quality metrics for our homology model and the two NMDAR template structures are provided in Fig. S5. An overlay of the model used for MD simulations with a recently published cryo-EM structure of a GluN1/GluN2A receptor is shown in Fig. S6. Table S1 provides the selected model structure and useful Python commands to help with renumbering of model residues.

Results

Sobolevsky et al. (2009) first proposed the idea that the pre-M1 helix could play a role in gating by acting as a cuff, based on the

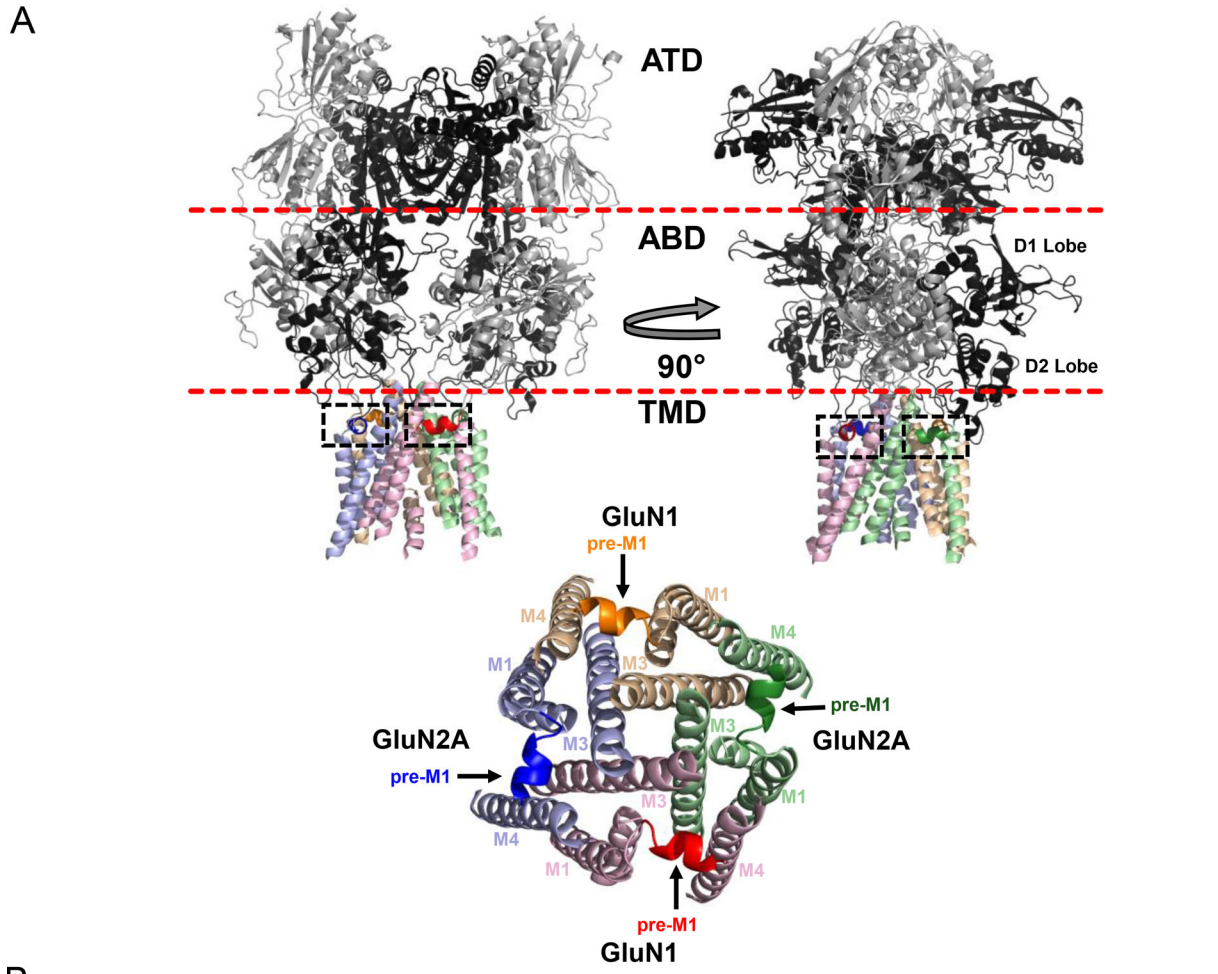

Figure 1. **Several aromatic residues around the pre-M1 helix are largely conserved across GluN subunits. (A)** Homology model of a GluN1/GluN2A NMDAR. GluN1 subunits are shown in gray, and GluN2A subunits are shown in black. The figure highlights the pre-M1 helices (black boxes) of GluN1 (orange and red helices) and GluN2A (blue and green helices) subunits. Top-down view illustrates the pre-M1 helices forming a cuff around the closed channel. **(B)** Sequence alignment of the pre-M1, M1, M3, and pre-M4 regions across human NMDAR subunits. The positions of aromatic residues of interest are shown in red. Highlighted (yellow) residues designate those which were mutated in our experiments, and gray boxes designate helical regions.

observation that it is in contact with the gate of the channel—the M3 helical bundle that occludes the pore in the closed state of a crystal structure of homomeric GluA2 (Fig. 1). Additionally, human de novo mutations are concentrated in this region (Ogden et al., 2017), suggesting that these residues play a central role in NMDAR gating that cannot be performed by other amino acids. To assess whether the residues of the pre-M1 helix play a role in controlling kinetically distinct pregating steps that reflect conformational changes that precede receptor opening, we designed a set of experiments guided by both functional studies of clinically relevant human mutations and limited structural data. We performed scanning mutagenesis of five residues constituting two turns of the GluN2A pre-M1 helix in which we substituted each residue for alanine and recorded the resultant macroscopic current response time course and single channel unitary currents to identify the contributions of individual residues to overall receptor function.

Effects of pre-M1 mutations on agonist potency and response time course

We expressed WT and mutant GluN2A subunits with the WT GluN1 subunit in *Xenopus* oocytes and determined the concentration–response relationship for glutamate and glycine. Of the mutants, GluN2A-F553A produced the largest effect on glutamate potency, showing a >10-fold decrease in the EC_{50} from 3.5 to 0.34 µM. The other mutations tested showed minimal

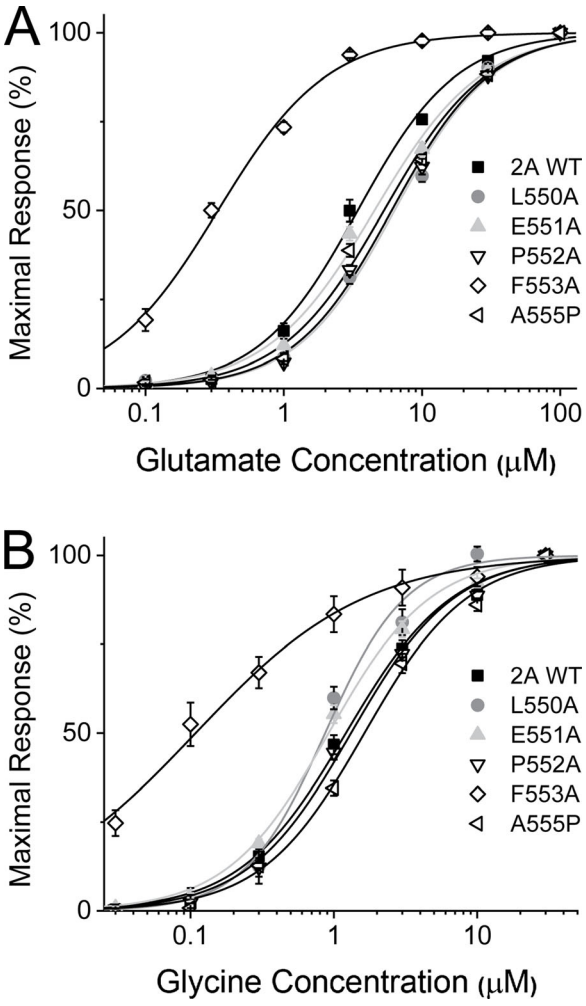

Figure 2. **Mutations in the GluN2 pre-M1 helix shift glutamate and glycine potency.** Steady-state concentration–response curves for glutamate in the presence of 100 μM glycine (A) and glycine in the presence of 100 μM glutamate (B). The Hill equation was fitted to the composite data for GluN2A WT and GluN2A-L550A, GluN2A-E551A, GluN2A-P552A, GluN2A-F553A, and GluN2A-A555P expressed with WT GluN1. GluN2A-F553A shifted glutamate potency ~11-fold (EC_{50} from 3.6 μM to 0.34 μM) and glycine potency ~18-fold (EC_{50} from 1.4 μM to 0.077 μM). Fitted EC_{50} values for all mutants can be found in Table 2.

effects on glutamate EC_{50}, with L550A, E551A, P552A, F553Y, and A555P changing glutamate potency by twofold or less (Fig. 2 A and Table 1). These results were mirrored by the findings for glycine potency, whereby GluN2A-F553A increased the glycine potency ~18-fold, shifting EC_{50} from 1.4 to 0.077 μM. Other pre-M1 mutations shifted potency by less than twofold (Fig. 2 B and Table 1). These results, where removing the aromatic side chain of Phe553 drastically alters the receptor response to agonist, suggest that this residue in particular may dictate the pre-M1 helix effects on channel gating.

If a conformational change in any part of the pre-M1 helix in response to agonist binding comprises a rate-limiting step that precedes pore dilation, then it might be expected that mutations in this region would alter the NMDAR activation or deactivation time course following rapid application and removal of glutamate. To test this idea, mutant and WT GluN2A subunits were coexpressed with the WT GluN1 subunit in HEK293 cells and whole-cell patch clamp recordings were conducted. HEK293 cells were maintained in solution with saturating glycine, and the response time course following brief coapplication of maximally effective glutamate plus glycine was measured for each GluN2A mutant. None of the mutants tested showed a significant difference in rise time compared with the WT GluN2A receptor. However, analysis of the deactivation time course following 1-s application and rapid removal of glutamate revealed that GluN2A-F553A prolonged the deactivation time course by ninefold, from 46 to 417 ms, whereas GluN2A-L550A accelerated deactivation by 3.5-fold, from 46 to 13 ms. The other GluN2A mutations produced only modest effects on the deactivation time course (Fig. 3 and Table 2). Additionally, GluN2A-L550A and GluN2A-F553A drastically reduced peak amplitude, while the other mutations had no observable effect.

Pre-M1 mutations alter NMDAR single channel properties

To assess the effects of pre-M1 mutations on channel properties, we recorded single ion channel currents in response to maximally effective concentrations of glutamate and glycine from cell-attached patches that contained one active channel (Colquhoun and Hawkes, 1990). Alanine substitutions at several positions caused a wide range of changes in the duration of prolonged shut periods, suggesting an impact on channel gating (Fig. 4, A–F and Table 3). Single channel activity was idealized into a sequence of openings and closings. The shut time histogram was fitted using the sum of four or five exponential components, and the slowest components used to identify a T_{crit} with which we could differentiate bursts from long closed states likely to reflect desensitization. This approach allowed for a more accurate interpretation of burst channel data without the potential for confounding results arising from mutation-specific effects on desensitization. When selecting bursts of channel openings based on a critical shut time (Jackson et al., 1983; Magleby and Pallotta, 1983), most of the alanine-substituted channels showed intraburst open probabilities that were similar to WT GluN2A (0.34; Table 3). By contrast, GluN2A-L550A and GluN2A-F553A, which reside on the same side of the helix, decreased open probability nearly 10-fold. Evaluation of the mean open time for each mutation revealed that GluN2A-L550A and GluN2A-F553A reduced the mean open time from 1.49 ms for the WT GluN2A receptor to 0.53 ms and 0.20 ms, respectively (Table 4). Evaluation of the mean shut times showed that both GluN2A-L550A and GluN2A-F553A increased the mean shut time, with GluN2A-L550A producing the largest shift from 29 to 900 ms (Table 5). These results suggest that multiple residues on one side of the short pre-M1 helix impact channel gating and implicate this region as critical for the gating control mechanism.

Previously, WT GluN1/GluN2A receptors have been reported to display multiple gating modes, higher open probability, and a longer mean open time when studied in the absence of extracellular calcium. (Popescu and Auerbach, 2004; Popescu et al., 2004). In this study, the single channel recordings were performed in the presence of 0.5 mM Ca^{2+}. The mean open time and

Table 1. **Summary of agonist EC_{50} values**

	Glutamate EC_{50} (μM)	Oocytes recorded (*n*)	Glycine EC_{50} (μM)	Oocytes recorded (*n*)
GluN2A WT	3.5 (2.9-4.2)	20	1.2 (0.99-1.5)	12
GluN2A-L550A	6.6 (6.0-7.3)[a]	17	0.84 (0.60-1.2)	11
GluN2A-E551A	4.8 (4.1-5.5)	18	0.93 (0.77-1.1)	12
GluN2A-P552A	6.4 (5.6-7.3)[a]	16	1.3 (1.1-1.6)	11
GluN2A-F553A	0.34 (0.30-0.38)[a]	19	0.12 (0.058-0.23)[a]	6
GluN2A-A555P	5.4 (4.7-6.1)[a]	18	1.6 (1.4-1.9)	11
GluN2A-F553Y	3.6 (3.1-4.1)	16	0.85 (0.68-1.1)	12
GluN2D WT	0.24 (0.20-0.30)	14	0.12 (0.091-0.15)	9
GluN2D-Y578F	0.43 (0.34-0.55)[a]	11	0.19 (0.14-0.25)	10

All data are from GluN1 coexpressed with GluN2A or GluN2D; the concentration–response curve for each recording was fitted by the Hill equation: *Response* (%) = $100/[1 + (EC_{50}/concentration)^H]$, where *H* is the Hill slope, which remained largely unchanged among mutants (1.2 ± 0.1). Data are presented as mean EC_{50} with the 95% confidence intervals in parentheses, determined from the log EC_{50} (two significant figures).
[a]Nonoverlapping 95% confidence intervals between mutant and WT receptor.

open probabilities reported here for WT GluN1/GluN2A receptors are consistent with those reported previously for the same receptors studied in the presence of extracellular calcium at pH 8.0 (Dravid et al., 2007; Chopra et al., 2015; Gibb et al., 2018).

The pre-M1 helix imparts distinguishing properties to GluN2C and GluN2D

While several residues of the pre-M1 helix are highly conserved across GluN2 subunits, the phenylalanine residue in position 553 is conserved in GluN1, GluN2A, and GluN2B, but corresponds to a tyrosine in GluN2C and GluN2D. Because the aromaticity of the phenylalanine in this position appears to be critical for receptor function, and this residue is the only difference between these subunits in this region, we questioned whether it could be responsible for their differences in open probability. To address this, we recorded single channel currents from GluN2A-F553Y, the GluN2C/D equivalent residue of GluN2A-Phe553. The GluN2A-F553Y receptors showed a slight reduction in glycine EC_{50} but showed no detectable differences from WT for glutamate EC_{50} (Fig. 5, A and B) or receptor response time course (Fig. 5 C) during brief application of a maximally effective concentration of glutamate in saturating glycine. Single channel analysis of GluN2A-F553Y revealed a 30% decrease in open probability compared with GluN2A WT (Fig. 5 D and Table 3), suggesting that the tyrosine at this pre-M1 site in GluN2C and GluN2D could contribute to the lower open probability of GluN2C- and GluN2D-containing receptors (Dravid et al., 2008; Vance et al., 2012), perhaps through potential hydrogen bond capability of tyrosine compared with phenylalanine.

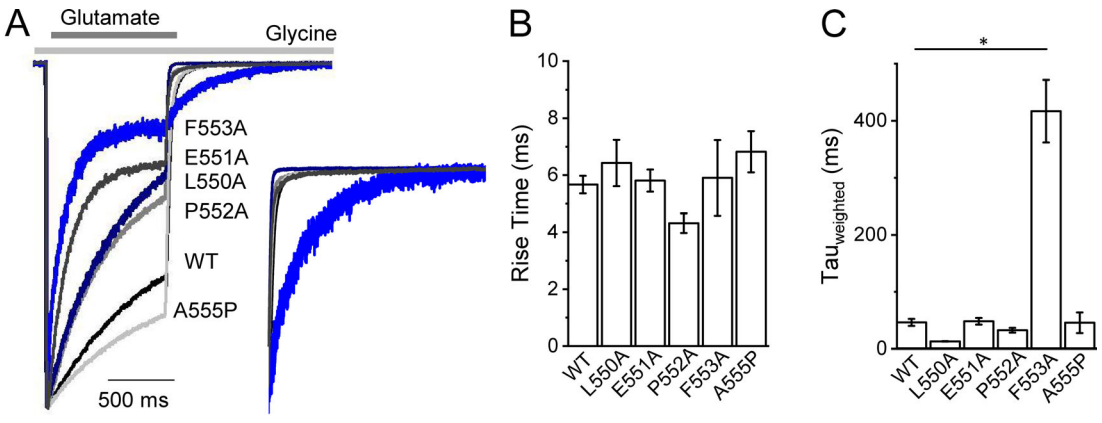

Figure 3. **GluN2A-F553A significantly prolongs the glutamate deactivation time course. (A)** Representative current response time course from whole-cell patch clamp recordings of WT and mutant GluN2A-containing receptors activated by a 1-s pulse of 1 mM glutamate in the continuous presence of 30 μM glycine. The response time courses are normalized to the peak current levels to allow for comparison of the desensitization time course. Inset: Current time course normalized to steady-state level on the same time base to allow comparison of the deactivation time course. **(B and C)** Average 10–90% rise times (B) and average weighted τ values (C) for WT and mutant GluN1/GluN2A receptors. The rise times did not differ significantly for any of the mutant subunits when compared with WT GluN2A. GluN2A-F553A prolonged deactivation time course by approximately ninefold from 46 ms to 417 ms. *, Significant difference from WT ($P < 0.05$ compared with WT 2A, one-way ANOVA, Tukey's post hoc test). A summary of fitted values can be found in Table 3.

Table 2. **Summary of deactivation time course for GluN2A mutations**

	Rise time (ms)	τ_{Fast} (ms)	τ_{Slow} (ms)	% τ_{Fast}	$_{Weighted}\tau$ (ms)	% Desensitization	Amplitude (peak, pA/pF)	*n*
GluN2A WT	5.7 ± 0.3	24 ± 2	180 ± 22	84 ± 3	46 ± 6	54 ± 5	190 ± 22	25
GluN2A-L550A	6.4 ± 0.8	11 ± 0.7	66 ± 24	93 ± 3	13 ± 0.4	30 ± 3	28 ± 2.6	12
GluN2A-E551A	5.8 ± 0.4	26 ± 3	220 ± 34	86 ± 3	48 ± 6	54 ± 5	220 ± 52	16
GluN2A-P552A	4.3 ± 0.3	16 ± 2	170 ± 15	87 ± 4	32 ± 4	31 ± 5	160 ± 14	12
GluN2A-F553A	5.9 ± 1	64 ± 16	790 ± 160	43 ± 6	420 ± 55[a]	18 ± 2	12 ± 1.5	9
GluN2A-A555P	6.8 ± 0.7	24 ± 2	190 ± 18	87 ± 4	46 ± 18	74 ± 7	170 ± 24	13
GluN2A-F553Y	5.5 ± 0.7	25 ± 2	230 ± 75	94 ± 2	37 ± 6	64 ± 5	79 ± 11	12

All data are from GluN1 co-expressed with GluN2A. Data are expressed as mean ± SEM to two significant figures.
[a]$P < 0.05$ compared with WT GluN2A, one-way ANOVA, Tukey's post hoc test. Analysis performed on rise time and weighted τ, and corrected for familywise error.

MTSEA modification of GluN1-A652C has been shown to lock NMDARs in an open state. Based on the assumption that open probability approaches 1 following covalent modification, we used the reciprocal relationship between the degree of potentiation and open probability to calculate the open probability (see Materials and methods). Introduction of the GluN2A-F553Y mutation was shown to significantly reduce the open probability 55% from 0.22 to 0.12 (Table 6). To support our hypothesis that this specific residue could account for differences in open probability between GluN2A and GluN2D receptors, we measured the changes in agonist potency and open probability of GluN2D-Y578F, the reciprocal substitution to GluN2A-F553Y. Both glutamate and glycine potency were reduced for the mutant receptor with glutamate EC_{50} shifting from 0.24 to 0.43 µM and glycine EC_{50} shifting from 0.12 to 0.19 µM (Table 1). Additionally, GluN2D-Y578F increased the open probability 33%, from 0.0055 to 0.0086 (Table 6). Together, these results support our hypothesis that the disparate residue identity at this position between GluN2A/GluN2B and GluN2C/GluN2D contributes in part to the difference in open probability between these subunits.

Subunit-specific pre-M1 helix interactions

A homology model of a GluN1a/GluN2A di-heteromeric structure was used to interpret the results presented thus far. Recently, several GluN1a/GluN2A structures were resolved using x-ray and cryo-EM techniques (Jalali-Yazdi et al., 2018; Zhang et al., 2018); however, none of these structures were available at the start of this study and were therefore not included. Three template structures were used in modeling of the GluN1a/GluN2A NMDAR. Two of the templates were that of the closely related GluN1/GluN2B NMDAR—PDB entries 4PE5 and 5FXH. PDB entry 4PE5 is an x-ray structure resolved at a resolution of 3.96 Å and was selected because it has a well-resolved ABD and ATD. However, there are two limitations of this structure: (1) the linker region between ABD and the TMD is not resolved; and (2), the TMD region only has the backbone residues resolved with no density for the side chains. The second template, PDB entry 5FXH, a cryo-EM structure resolved at 5 Å, was selected because it has a resolved linker region between the ABD and TMD. This template is limited in that only the backbone residues are resolved, but it allowed us to build in the linker region. The third template used, an x-ray PDB entry 5L1B (resolution 4.0 Å), is an AMPAR structure from which the ATD and ABD were removed in the model building process. This template was selected to build in missing residues of GluN2B structures in the TMD. The TMDs of GluN1/GluN2B and AMPA show a 3.5-Å RMSD when aligned on the backbone structures and shares a 30.3% (GluN1) and 27.6% (GluN2) sequence identity within this region. The GluN1 template structures share 92.2% and 94.5% sequence identity with GluN1a target sequence used to build the GluN1a/GluN2A (Fig. S3). The GluN2B template structures share a 64.0% and 69.1% sequence identity with the GluN2A target structure used in model generation (Fig. S4).

The five homology models had molpdf values ranging from 87,071 to 92,375, from which the lowest relative energy model was selected for further analysis. This selected model showed a G-factor of −0.06 (values less than −0.5 are unusual), suggesting good overall stereochemistry of the model. The Ramachandran plot was found to be similar to that of templates PDB identifiers 5FXH and 4PE5 and showed 89.7% of the residues in the most favored regions, 8.7% in additional allowed areas, 0.8% in generously allowed regions, and 0.7% in disallowed regions (none of the latter were found in the pre-M1 helix; total of 3,196 amino acids; Fig. S5). The slightly elevated value for residues in the disallowed region highlights that caution should be taken when interpreting results from the models and subsequent MD simulations even though the value is similar to the observed frequency (0.5%) in the PDB (Gore et al., 2017). These results give us confidence in the quality of the model generated in this study. Finally, we measured the backbone RMSD of the GluN2A model lacking the ATD from a newly released cryo-EM structure (PDB identifier 6IRA; Zhang et al., 2018) which gave a value of 3.7 Å (across ∼4,700 atoms) when aligned on the entire model and had a range between 2.5 and 2.9 Å (across ∼1,500 atoms) when aligned on each chain independently (Fig. S6).

The results presented thus far suggest that the aromaticity of the amino acid residue at position 553 of GluN2A is critical for normal function of GluN2A-containing NMDARs. To explore the mechanism by which this side chain contributes to channel

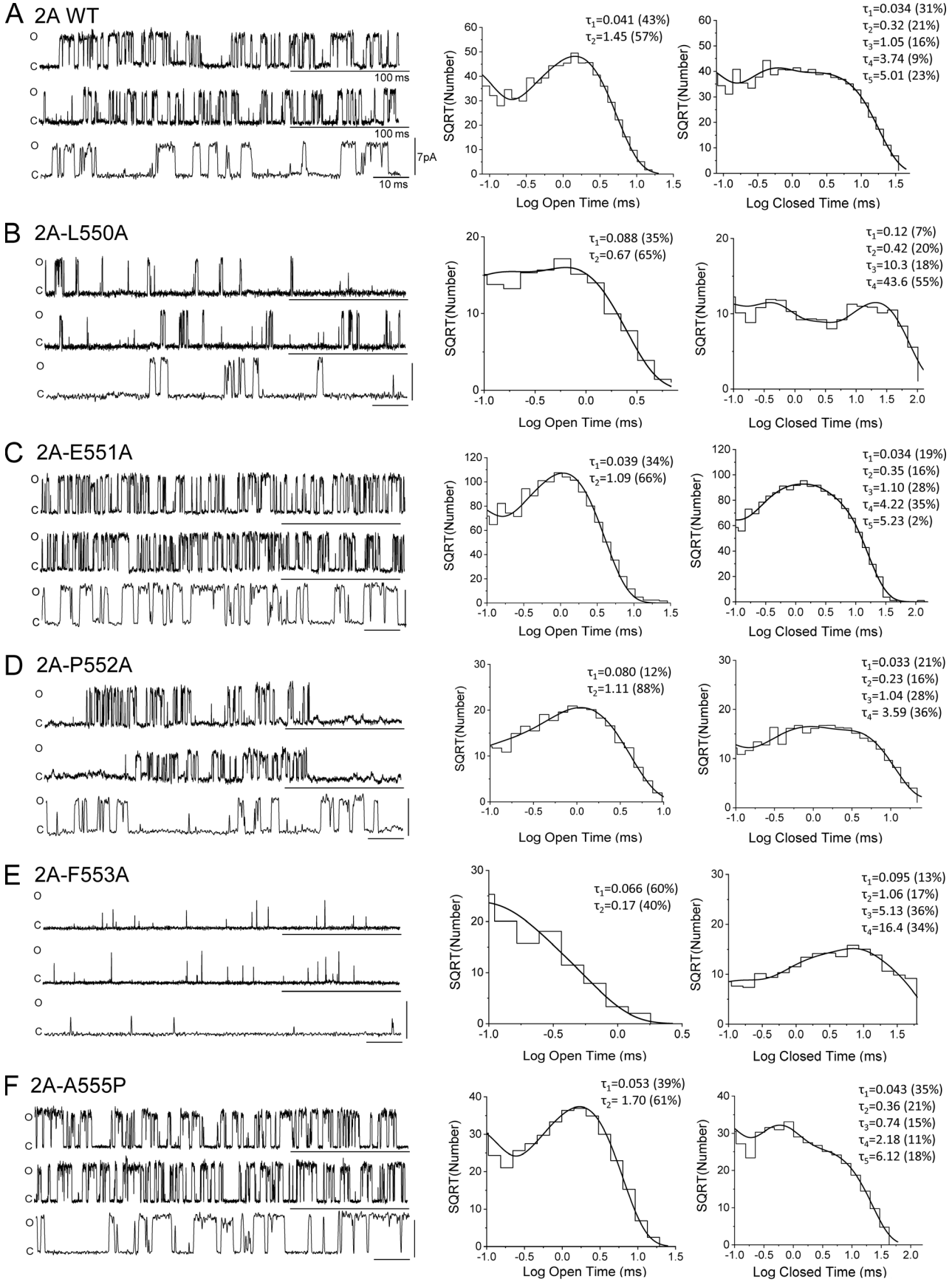

Figure 4. **GluN2A-L550A and GluN2A-F553A significantly alter single channel properties. (A–F)** Representative single channel unitary currents from cell-attached patches that contained one active WT or mutant GluN1/GluN2A NMDAR activated by 1 mM glutamate and 50 µM glycine. All currents are displayed on the same scale. Representative histograms are shown on a square root-log scale; open time histograms were fitted (maximum likelihood) with two exponential functions and shut time histograms were fitted with four or five exponential functions.

gating, we performed MD simulations over a 250-ns time scale to allow residues in the model to relax to a steady-state position. Analysis revealed a complex network of aromatic residues that were coordinated around GluN2A-Phe553 and included residues Phe810 of the GluN1 pre-M4 linker, Phe641, Tyr645 of the GluN2A M3 transmembrane helix, and Trp558 of the GluN2A M1 transmembrane helix (Fig. 6 B). The simulation places Phe553 near the middle of this aromatic network within a range permissible to both edge-to-face and face-to-face π–π stacking. Specifically, our simulation showed that the centroid of the aromatic ring of GluN2A-Phe553 is a mean distance of 6.6, 5.9, and 5.4 Å from the ring centroids of GluN1-Phe810, GluN2A-Tyr645, and GluN2A-Trp558, respectively. In addition, GluN2A-Phe641 is within 5.7 Å of GluN2A-Phe637 and 5.7 Å from GluN1-Phe817. Histograms showing the full range of distances observed during the 250-ns simulation are provided in Fig. S2. All these reported distances are shorter than the "strict" π–π interaction distance of 6.5 Å for large biomolecules derived from a survey of the entire PDB (Piovesan et al., 2016), with the exception of the mean distance between GluN2A-Phe553 and GluN1-Phe810, which still falls within the "relaxed" threshold of 7.0 Å. Distances between the β-carbons can be found in Fig. S2.

To explore how this aromatic network might be disrupted upon substitution of GluN2A-Phe553 with alanine, we repeated the 250-ns MD simulation with the introduction of this single mutation (Fig. 6 D). Without the presence of the phenylalanine aromatic side chain at position 553, the aromatic network is disrupted and shows increased distances between the C_β of GluN2A-Trp558, GluN2A-Tyr645, and GluN1-Phe810 from that of the central residue, GluN2A-Ala553, compared with the WT (1.5, 2.5, and 3.2 Å, respectively). We hypothesize that this disruption interferes with communication between the pre-M1 helix and both the M3 helix and the adjacent GluN1 subunit. This finding supports the electrophysiological data in that the receptor's ability to open or close is altered if interactions between the ligand-binding domain–tethered pre-M1 helix and the channel pore are disrupted.

Many of these aromatic residues are conserved across NMDAR subunits (Fig. 1 B), implying that the interactions between these residues is similarly conserved. However, the GluN1 pre-M1 helix appears to participate in gating in a manner distinct from that of GluN2A, as suggested by results showing that mutations in the GluN1 pre-M1 helix do not slow receptor activation, while their GluN2 counterparts do (Ogden et al., 2017; Gibb et al., 2018). We therefore investigated the amino acid environment surrounding the GluN1-Phe558 residue (Fig. 6 C). We found that GluN1-Trp563 is within 7.4, 6.2, and 5.8 Å of GluN1-Tyr647, GluN1-Phe554, and GluN1-Phe558, respectively. GluN1-Tyr647 corresponds to GluN2A-Tyr645 and GluN1-Trp563 corresponds to GluN2A-Trp558. Additionally, the GluN1 equivalent of GluN2-Phe651 and the GluN2 equivalent of GluN1-Phe810 are both replaced by isoleucine, which is incapable of participating in the aromatic network. Comparison of the set of GluN1-Phe558 and GluN2A-Phe553 aromatic interactions might explain why disease-associated mutations in GluN2A do not have

Table 3. **Summary of single channel data for GluN2A mutations**

	Events (*n*)	Burst P_{open}	Burst mean open time (ms)	Burst mean shut time (ms)	Shut time T_{crit} (ms)	*n*
GluN2A WT	315,130	0.34 ± 0.008	1.5 ± 0.1	2.9 ± 0.2	31 ± 2	6
GluN2A-L550A	6,519	0.033 ± 0.006[a]	0.66 ± 0.05[a]	22 ± 3	155 ± 13	7
GluN2A-E551A	307,463	0.38 ± 0.04	1.3 ± 0.1	2.3 ±0.3	24 ± 2	3
GluN2A-P552A	17,623	0.34 ± 0.02	1.3 ± 0.06	2.5 ± 0.2	25 ± 3	7
GluN2A-F553A	3,484	0.020 ± 0.005[a]	0.21 ± 0.007[a]	12 ± 3	59 ± 6	3
GluN2A-A555P	74,905	0.39 ± 0.06	1.7 ± 0.1	2.8 ± 0.5	38 ± 9	3
GluN2A-F553Y	67,723	0.23 ± 0.02[a]	1.4 ± 0.15	4.6 ± 0.07	48 ± 5	3

All data are from GluN1 coexpressed with GluN2A. Data expressed as mean ± SEM to two significant figures. P_{open}, open probability.
[a]$P < 0.05$ compared with WT GluN2A, one-way ANOVA, Tukey's post hoc test, corrected for familywise error for P_{open} and burst mean open time.

Table 4. **Open dwell time analysis for GluN2A mutations**

	τ_1 (ms)	$Area_1$ (%)	τ_2 (ms)	$Area_2$ (%)	Patches (*n*)
GluN2A WT	0.053 ± 0.005	41 ± 4	1.6 ± 0.14	59 ± 4	6
GluN2A-L550A	0.081 ± 0.015	47 ± 4	0.68 ± 0.060	53 ± 5	6
GluN2A-E551A	0.045 ± 0.003	26 ± 5	1.3 ± 0.11	75 ± 5	3
GluN2A-P552A	0.059 ± 0.007	29 ± 5	1.2 ± 0.042	72 ± 5	6
GluN2A-F553A	0.050 ± 0.009	58 ± 3	0.16 ± 0.007	42 ± 3	3
GluN2A-A555P	0.053 ± 0.006	35 ± 8	1.6 ± 0.080	65 ± 8	3
GluN2A-F553Y	0.048 ± 0.007	52 ± 3	1.5 ± 0.23	48 ± 3	3

Open time distributions were fitted (maximum likelihood) by two exponential components. Fitted parameters are expressed as mean ± SEM to two significant figures.

Table 5. **Closed dwell time analysis for GluN2A mutations**

	τ_1 (ms)	$Area_1$ (%)	τ_2 (ms)	$Area_2$ (%)	τ_3 (ms)	$Area_3$ (%)	τ_4 (ms)	$Area_4$ (%)	τ_5 (ms)	$Area_5$ (%)	Patches (*n*)
GluN2A WT	0.037 ± 0.002	27 ± 2	0.31 ± 0.029	20 ± 1	1.1 ± 0.18	17 ± 12	2.3 ± 0.32	8 ± 3	5.1 ± 0.22	28 ± 2	6
GluN2A-L550A	0.088 ± 0.012	21 ± 3	–	–	0.70 ± 0.21	18 ± 2	9.5 ± 1.6	19 ± 5	36 ± 3.7	41 ± 5	7
GluN2A-E551A	0.035 ± 0.0002	21 ± 2	0.33 ± 0.010	15 ± 1	1.1 ± 0.033	31 ± 5	3.8 ± 0.31	22 ± 8	4.2 ± 0.58	11 ± 5	3
GluN2A-P552A	0.041 ± 0.004	25 ± 4	0.36 ± 0.071	22 ± 3	1.4 ± 0.18	24 ± 9	4.7 ± 0.33	29 ± 4	–	–	6
GluN2A-F553A	0.058 ± 0.018	11 ± 1	–	–	1.1 ± 0.054	16 ± 2	7.5 ± 2.6	36 ± 5	14 ± 1.8	37 ± 7	3
GluN2A-A555P	0.049 ± 0.007	27 ± 4	0.54 ± 0.16	25 ± 2	1.1 ± 0.26	21 ± 8	3.8 ± 0.86	20 ± 8	9.6 ± 3.4	11 ± 7	3
GluN2A-F553Y	0.034 ± 0.0003	31 ± 4	0.30 ± 0.021	17 ± 1	2.5 ± 0.67	13 ± 3	5.4 ± 1.2	5 ± 1	12 ± 4.7	16 ± 9	3

Closed time distributions were fitted (maximum likelihood) by four to five exponential components. Fitted parameters are expressed as mean ± SEM to two significant figures.

the same functional consequences when expressed in GluN1 (Ogden et al., 2017; Gibb et al., 2018). Because the aromatic network that potentially dictates channel gating is less extensive in GluN1 pre-M1 helix, mutations in this region might have reduced functional consequences.

Discussion

In this study, we investigated the role of the GluN2A pre-M1 helix in channel gating. We found the GluN2A residue Phe553 to be particularly critical for channel function as indicated by significant changes to both macroscopic and single channel

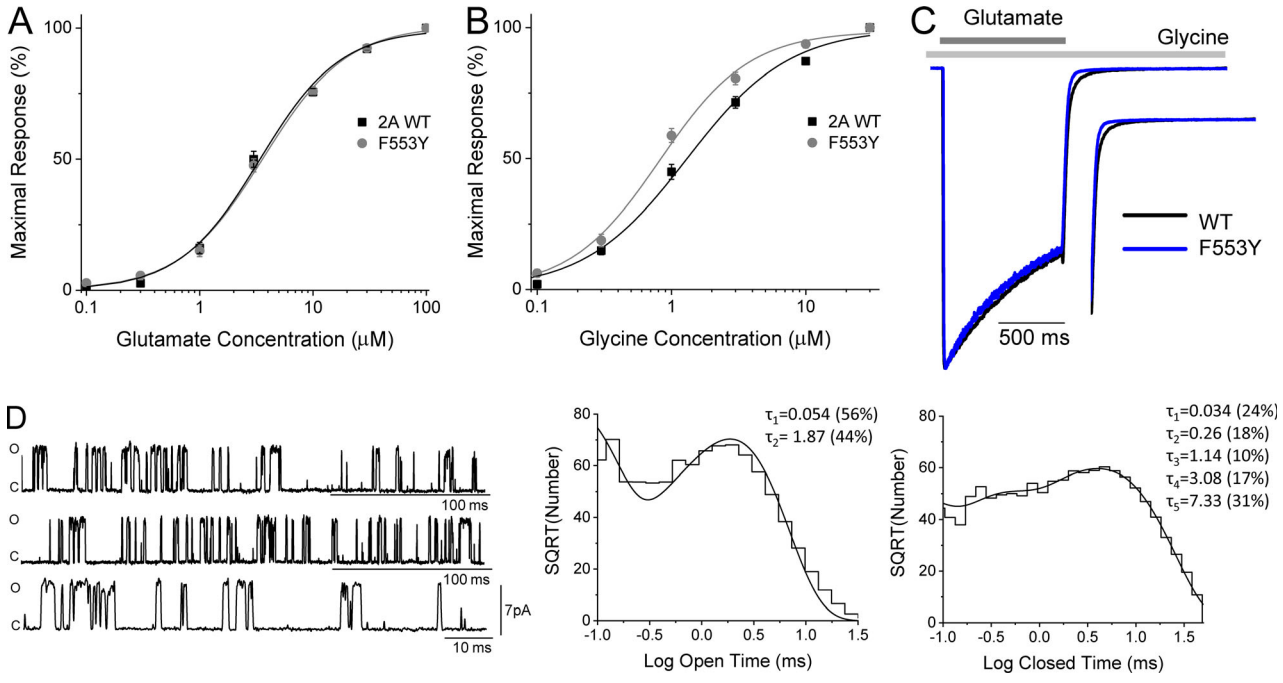

Figure 5. **Substitution of GluN2A Phe553 with Tyr reduces the open probability but has no detectable effect on macroscopic properties. (A and B)** Steady-state concentration–response curves for glutamate in the presence of 100 µM glycine (A) and glycine in the presence of 100 µM glutamate (B) for WT GluN2A and GluN2A-F553Y. **(C)** Representative current responses from whole-cell patch clamp recordings of WT GluN2A and GluN2A-F553Y activated by a 1-s pulse of 1 mM glutamate in the continued presence of 30 µM glycine. Inset: Current response time course normalized to steady state to show deactivation. **(D)** Representative single channel unitary currents recorded from cell-attached patches containing one active GluN1/GluN2A-F553Y receptor activated by 1 mM glutamate and 50 µM glycine. Representative histograms for the open time are shown on a log-square root scale and were fitted (maximum likelihood) with two exponential functions; shut time histograms were fitted with five exponential functions.

Table 6. **Oocyte MTSEA calculated open probability**

	Calculated P_{open}	Oocytes recorded (*n*)
GluN2A WT	0.22 ± 0.007	8
GluN2A-F553Y	0.12 ± 0.008[a]	10
GluN2D WT	0.0055 ± 0.0007	12
GluN2D-Y578F	0.0086 ± 0.0005[a]	12

All data are from GluN1 coexpressed with GluN2A or GluN2D. P_{open} was calculated according to the equation given in Materials and methods. Data are expressed as mean ± SEM.
[a]$P < 0.05$ compared with WT, unpaired *t* test.

properties. Moreover, we used MD simulations to probe the mechanism by which this residue might contribute to gating. Our analysis revealed a network of aromatic amino acids within the π-stacking range surrounding GluN2A-Phe553 that was disrupted by alanine substitution at this position.

Specifically, we conducted scanning mutagenesis of the pre-M1 helix to investigate the effects on various receptor properties. Of the mutants tested, GluN2A-F553A presented the greatest effect on glutamate and glycine EC_{50}, showing an ∼11-fold and an ∼18-fold increase in potency, respectively. That is, GluN2A-F553A shifted the potency of both NMDAR agonists, despite only being introduced to the GluN2A subunit. In addition, GluN2A-F553A prolonged the weighted deactivation time course by approximately ninefold, reduced peak amplitude by ∼16-fold, decreased open probability by ∼10-fold, and reduced the mean open time by approximately sevenfold. GluN2A-L550A, situated on the same side of the pre-M1 helix as GluN2A-Phe553, also altered single channel properties, decreasing open probability by ∼10-fold, increasing the mean open time by approximately threefold, and increasing the mean closed time by ∼30-fold. Together, these results suggest that these two amino acids in GluN2A (Leu550 and Phe553) control channel gating in a manner that is likely dependent upon their

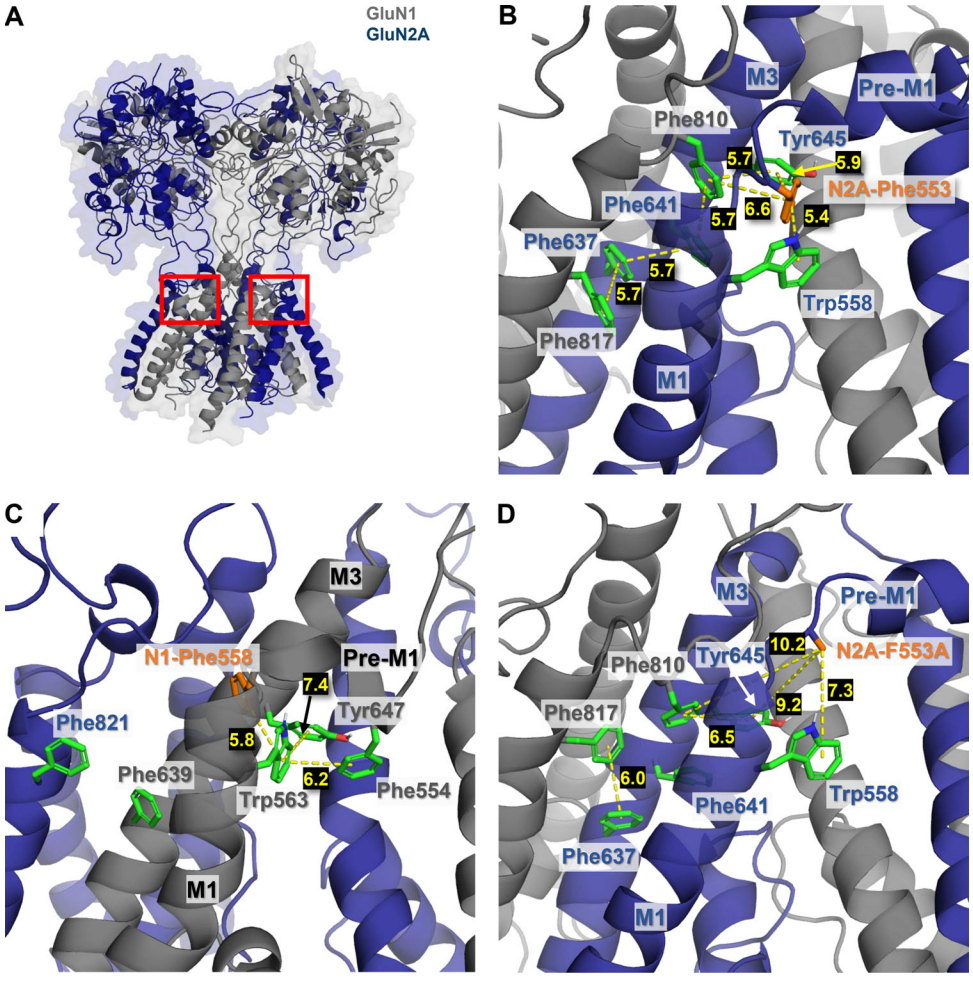

Figure 6. **A network of aromatic residues around GluN2A-Phe553 and GluN1-Phe558. (A)** Homology model used for the simulations with the ATD truncated. **(B)** A model of GluN2A (blue) and GluN1 (gray) at the 217.8-ns time point in the MD simulation showing seven potential interactions among aromatic residues, including GluN2A-Phe553; all interactions are within the range of favorable distances for π–π interactions (Piovesan et al., 2016). **(C)** WT GluN1 at the 185.6-ns time point showing a less extensive network of aromatic residues surrounding GluN1-Phe558. **(D)** GluN1/GluN2A-F553A at the 227.8-ns time point showing that this mutation disrupts the aromatic network found in the WT receptor. All time points shown represent the centroid structure from the largest cluster of frames over the equilibrated 250-ns GluN2A WT and GluN2A-F553A simulations (see Materials and methods). Yellow dashed lines represent the average distance (in Ångstroms) between the centers of aromatic rings across this same 250-ns period; histograms of these distances are found in Fig. S2.

structural contacts with residues adjacent to their side of the pre-M1 helix. Additionally, these results may also provide mechanistic context for the previously characterized disease-associated mutations GluN1-P557R, GluN2A-P552R, and GluN2B-P553L in this region (Ogden et al., 2017).

Our single channel recordings were performed in 0.5 mM Ca^{2+}, which can have a profound effect on single channel properties. The open probability we report here for the WT GluN2A receptor (0.34) is consistent with those determined in the presence of Ca^{2+} in cell-attached patches (Dravid et al., 2007; Iacobucci and Popescu, 2017) and in outside-out patches (Gibb et al., 2018; Rycroft and Gibb, 2002; Bhattacharya et al., 2018). Moreover, Iacobucci and Popescu (2017) show the open probability drops by threefold from 0.62 (0 mM Ca^{2+}) to 0.21 (0.5 mM Ca^{2+}), suggesting that the lack of divalent ions in previously published cell-attached patch studies contributes to the higher open probability observed in the absence of extracellular Ca^{2+} (Popescu et al., 2004).

GluN2A-Phe553 has previously been investigated for its role in desensitization. In AMPARs, a leucine resides at this position, perhaps suggesting that the amino acid at this position contributes to the differences in desensitization between these two families of ionotropic glutamate receptors. When GluN1-Phe558—the equivalent of GluN2A-Phe553—was substituted with leucine and expressed with WT GluN2A, the receptor retained its GluN2A-like desensitization phenotype. However, when GluN2A-F553L or GluN2B-F554L was expressed with WT GluN1, the desensitization resembled that of the AMPAR (Alsaloum et al., 2016). It was proposed, therefore, that the mechanism of desensitization in NMDARs differs from that of AMPARs as a result of differences between the composition of a hydrophobic box made up of aromatic residues within pre-M1 and M3. While this finding emphasizes the importance of receptor-specific hydrophobic boxes in functional divergence between the ionotropic glutamate receptors, it does not address the functional differences between GluN1 and GluN2 subunits suggested by the finding that the homologous F553L mutation in GluN1 was not sufficient to alter desensitization.

Interestingly, when GluN2A-Phe553 was substituted with tyrosine, the GluN2C and GluN2D amino acid equivalent, we found no measurable effect on desensitization as previously reported (Krupp et al., 1998; Alsaloum et al., 2016), suggesting that the pre-M1 segment cannot account for differences in desensitization between different GluN2 subunits. Our results show that, while GluN2A-F553Y had no significant effect on macroscopic properties, this mutation significantly reduced open probability, consistent with the reduced open probability of GluN2C- and GluN2D-containing receptors. We found that GluN2D-Y578F reduced glutamate potency, reduced glycine potency, and increased open probability as determined by MTSEA relative to the WT GluN2D receptor. These findings suggest that, in addition to being critical for the gating mechanism, the identity of the residue at position 553 can impart subunit-specific single channel properties to the receptor. The hydroxyl group of the tyrosine in this position for GluN2C and GluN2D receptors may introduce a hydrogen bond that is absent from GluN2A and GluN2B receptors. One possibility for such a hydrogen bond interaction, as predicted from sidechain positions in the MD simulations, could be between the hydroxyl group of the tyrosine at this site in the pre-M1 and the tyrosine of the SYTANLAAF motif (Y645 in GluN2A; Fig. 6 B). Additionally, the GluN2A-Ala555 residue is not conserved across the NMDA subunits. In GluN2C and GluN2D, the residue in this position is a proline, as tested in our experiments. However, as our data show, the GluN2A-A555P mutation was not sufficient on its own to produce significant changes to macroscopic or single channel properties of the receptor, suggesting that pre-M1 control of single channel properties is specific to the residue at position 553.

The side of the helix that harbors GluN2A-Leu550 and GluN2A-Phe553 appears to be oriented toward the SYTANLAAF-conserved helical bundle and the pre-M4 helix of the adjacent subunit (Chen et al., 2017). That is, the residues that were of consequence during our scanning mutagenesis study are positioned toward the triad that has been proposed to control channel gating (Gibb et al., 2018). Our findings, taken with the results from Alsaloum et al. (2016), suggest that the phenylalanine of the pre-M1 helix, despite being critical for channel gating and desensitization, differs in function among GluN subunits, likely as a result of differences in local residues with which this region can interact.

We used MD to explore the hydrophobic network in the context of pre-M1 scanning mutagenesis to identify potential roles for pre-M1 that could account for differences in gating control between GluN1 and GluN2. Using a GluN2A homology model built from a GluN2B crystal and cryo-EM structures, as well as the TMD of a closed AMPA structure, we examined the amino acid environment surrounding the pre-M1 helix. Within the GluN2A subunit, Phe553 is surrounded by a network of aromatic amino acids composed of GluN2A-Phe641 and GluN2A-Tyr645 of the GluN2A M3 helix, GluN2A-Trp558 of the GluN2A M1 helix, and GluN1-Phe810 of the neighboring GluN1 pre-M4 helix. When we repeated the simulation with an alanine substituted at the position of GluN2A-Phe553, we observed a disruption of the aromatic network and an increase in the distances from the ring centroids of GluN2A-Tyr645 and GluN2A-Trp558 to the 553 position. This supports the hypothesis that the aromatic network is critical for channel function and disruption of this network can perturb channel function. Finally, a comparison of the GluN1 aromatic network with that observed for GluN2A revealed a reduction in the number of interacting residues in GluN1, suggesting that the network plays a unique role in the GluN2A subunit.

Previous findings show that some of the residues close enough to contact GluN2A-Phe553 also influence channel function and gating, which lends credibility to the idea that the aromatic amino acid network controls gating in the NMDAR. First, the disease-associated mutation GluN2A-W558S was identified in a patient with epilepsy (ClinVar; available from https://www.ncbi.nlm.nih.gov/clinvar). Within the M3 helix, GluN2A-Phe637 has been shown to influence agonist potency and channel gating (Ren et al., 2007), and GluN1-Y647S has been identified in a patient with infantile spasms (Allen et al., 2013). In the M4 helix, GluN1-F817L has been identified in a patient with intellectual

disability, developmental delay, and movement disorder (Lemke et al., 2016; Zhu et al., 2015). Although these disease-associated mutations have not been functionally characterized, their potential role in these neurological disorders suggest that they likely disrupt normal NMDAR function.

In 2018, 23 full-length structures of the heteromeric GluN2A receptor were resolved (4.5–16.5 Å) using cryo-EM, none of which had resolution covering the complete transmembrane and linker regions (Zhang et al., 2018; Jalali-Yazdi et al., 2018). Some structures showed resolution within the pre-M1 helix region; however, they showed high B-factor values (358–515). When we compared the two GluN2A chains, Phe553 and Leu550 had different positions on the chains (B and D), suggesting uncertainty within the structures. We therefore opted to use homology models and not the cryo-EM GluN2A structures for calculations. Future studies however could benefit from incorporating the cryo-EM GluN2A structures in conjunction with AMPAR structures as templates to build homology models. The homology models generated were from crystal and cryo-EM structures that had resolution within the pre-M1 and linker regions. We used the well-resolved transmembrane region of the AMPAR, which has high sequence homology and structural similarity to the transmembrane regions of GluN1 and GluN2A.

Overall, the results from this study emphasize the previously suggested role of the pre-M1 helix in channel gating by demonstrating how specific residues within this region are critical for channel function. In addition, these results implicate the surrounding amino acid environment in the mechanism of channel gating by revealing a network of aromatic residues that is disrupted by an alanine substitution at the central phenylalanine residue. Finally, these results suggest unique subunit-specific contributions of pre-M1 helices in GluN1 and GluN2 to channel gating due to nonequivalent gating triads.

Acknowledgments

Merritt C. Maduke served as editor.

This work was supported by the National Institute of Neurological Disorders and Stroke, National Institutes of Health (grants R01-NS036654 and R35-NS111619-01 to S.F. Traynelis and grant F31-NS106896 to M.J. McDaniel).

S.F. Traynelis is a primary investigator on research grants from Biogen and Janssen to Emory University School of Medicine; is a member of the Scientific Advisory Board for Sage Therapeutics, the GRIN2B Foundation, and the CureGRIN Foundation; is cofounder of NeurOp, Inc.; and receives royalties for software. D.C. Liotta is a member of the Board of Directors for NeurOp, Inc. D.C. Liotta and S.F. Traynelis are coinventors of Emory-owned intellectual property that includes allosteric modulators of NMDA receptor function. P.B. Burger is a cofounder of Avicenna Biosciences, LLC.

Author contributions: M.J. McDaniel designed and performed experiments, performed analysis, and wrote the paper. K.K. Ogden designed and performed experiments, performed analysis, and wrote the paper. S.A. Kell designed experiments, performed simulations, performed analysis, and wrote the paper. P.B. Burger designed experiments, performed simulations, performed analysis, and wrote the paper. D.C. Liotta designed experiments and wrote the paper. S.F. Traynelis designed experiments, performed analysis, and wrote the paper.

Submitted: 1 March 2019
Revised: 9 August 2019
Accepted: 14 February 2020

References

Allen, A.S., S.F. Berkovic, P. Cossette, N. Delanty, D. Dlugos, E.E. Eichler, M.P. Epstein, T. Glauser, D.B. Goldstein, Y. Han, et al. Epilepsy Phenome/Genome Project. 2013. De novo mutations in epileptic encephalopathies. *Nature.* 501:217–221. https://doi.org/10.1038/nature12439

Alsaloum, M., R. Kazi, Q. Gan, J. Amin, and L.P. Wollmuth. 2016. A molecular determinant of subtype-specific desensitization in ionotropic glutamate receptors. *J. Neurosci.* 36:2617–2622. https://doi.org/10.1523/JNEUROSCI.2667-15.2016

Amin, J.B., G.R. Moody, and L.P. Wollmuth. 2020. From bedside-to-bench: What disease-associated variants are teaching us about the NMDA receptor. *J. Physiol.* In press. https://doi.org/10.1113/JP278705

Armstrong, N., and E. Gouaux. 2000. Mechanisms for activation and antagonism of an AMPA-sensitive glutamate receptor: crystal structures of the GluR2 ligand binding core. *Neuron.* 28:165–181. https://doi.org/10.1016/S0896-6273(00)00094-5

Beck, C., L.P. Wollmuth, P.H. Seeburg, B. Sakmann, and T. Kuner. 1999. NMDAR channel segments forming the extracellular vestibule inferred from the accessibility of substituted cysteines. *Neuron.* 22:559–570. https://doi.org/10.1016/S0896-6273(00)80710-2

Bhattacharya, S., A. Khatri, S.A. Swanger, J.O. DiRaddo, F. Yi, K.B. Hansen, H. Yuan, and S.F. Traynelis. 2018. Triheteromeric GluN1/GluN2A/GluN2C NMDARs with unique single-channel properties are the dominant receptor population in cerebellar granule cells. *Neuron.* 99:315–328.e5. https://doi.org/10.1016/j.neuron.2018.06.010

Burger, P., and S. Kell. 2020. MD Simulations HsGluN1/GluN2A WT/F553A. https://zenodo.org/record/3633408#.XmZaMqhKiUk https://doi.org/10.5281/zenodo.3633408

Chang, H.R., and C.C. Kuo. 2008. The activation gate and gating mechanism of the NMDA receptor. *J. Neurosci.* 28:1546–1556. https://doi.org/10.1523/JNEUROSCI.3485-07.2008

Chen, C., and H. Okayama. 1987. High-efficiency transformation of mammalian cells by plasmid DNA. *Mol. Cell. Biol.* 7:2745–2752. https://doi.org/10.1128/MCB.7.8.2745

Chen, W., C. Shieh, S.A. Swanger, A. Tankovic, M. Au, M. McGuire, M. Tagliati, J.M. Graham, S. Madan-Khetarpal, S.F. Traynelis, et al. 2017. GRIN1 mutation associated with intellectual disability alters NMDA receptor trafficking and function. *J. Hum. Genet.* 62:589–597. https://doi.org/10.1038/jhg.2017.19

Chopra D, M. Irvine, D. Jane, D. Monaghan, and S. Dravid. 2015. Gating effects of a novel allosteric modulator at GluN1/GluN2A NMDA receptors. *FASEB J.* 29:933.3.

Clements, J.D. 1996. Transmitter timecourse in the synaptic cleft: its role in central synaptic function. *Trends Neurosci.* 19:163–171. https://doi.org/10.1016/S0166-2236(96)10024-2

Colquhoun, D., and A.G. Hawkes. 1990. Stochastic properties of ion channel openings and bursts in a membrane patch that contains two channels: evidence concerning the number of channels present when a record containing only single openings is observed. *Proc. R. Soc. Lond. B Biol. Sci.* 240:453–477. https://doi.org/10.1098/rspb.1990.0048

Coyle, J.T. 2006. Glutamate and schizophrenia: beyond the dopamine hypothesis. *Cell. Mol. Neurobiol.* 26:365–384. https://doi.org/10.1007/s10571-006-9062-8

Cull-Candy, S., S. Brickley, and M. Farrant. 2001. NMDA receptor subunits: diversity, development and disease. *Curr. Opin. Neurobiol.* 11:327–335. https://doi.org/10.1016/S0959-4388(00)00215-4

Dolino, D.M., S. Chatterjee, D.M. MacLean, C. Flatebo, L.D.C. Bishop, S.A. Shaikh, C.F. Landes, and V. Jayaraman. 2017. The structure-energy landscape of NMDA receptor gating. *Nat. Chem. Biol.* 13:1232–1238. https://doi.org/10.1038/nchembio.2487

Dravid, S.M., K. Erreger, H. Yuan, K. Nicholson, P. Le, P. Lyuboslavsky, A. Almonte, E. Murray, C. Mosely, J. Barber, et al. 2007. Subunit-specific

mechanisms and proton sensitivity of NMDA receptor channel block. *J. Physiol.* 581:107–128. https://doi.org/10.1113/jphysiol.2006.124958

Dravid, S.M., A. Prakash, and S.F. Traynelis. 2008. Activation of recombinant NR1/NR2C NMDA receptors. *J. Physiol.* 586:4425–4439. https://doi.org/10.1113/jphysiol.2008.158634

Edgar, R.C. 2004. MUSCLE: multiple sequence alignment with high accuracy and high throughput. *Nucleic Acids Res.* 32:1792–1797. https://doi.org/10.1093/nar/gkh340

Furukawa, H., and E. Gouaux. 2003. Mechanisms of activation, inhibition and specificity: crystal structures of the NMDA receptor NR1 ligand-binding core. *EMBO J.* 22:2873–2885. https://doi.org/10.1093/emboj/cdg303

Furukawa, H., S.K. Singh, R. Mancusso, and E. Gouaux. 2005. Subunit arrangement and function in NMDA receptors. *Nature.* 438:185–192. https://doi.org/10.1038/nature04089

Gibb, A.J., K.K. Ogden, M.J. McDaniel, K.M. Vance, S.A. Kell, C. Butch, P. Burger, D.C. Liotta, and S.F. Traynelis. 2018. A structurally derived model of subunit-dependent NMDA receptor function. *J. Physiol.* 596:4057–4089. https://doi.org/10.1113/JP276093

Gore, S., E. Sanz García, P.M.S. Hendrickx, A. Gutmanas, J.D. Westbrook, H. Yang, Z. Feng, K. Baskaran, J.M. Berrisford, B.P. Hudson, et al. 2017. Validation of Structures in the Protein Data Bank. *Structure.* 25:1916–1927. https://doi.org/10.1016/j.str.2017.10.009

Hansen, K.B., N. Tajima, R. Risgaard, R.E. Perszyk, L. Jørgensen, K.M. Vance, K.K. Ogden, R.P. Clausen, H. Furukawa, and S.F. Traynelis. 2013. Structural determinants of agonist efficacy at the glutamate binding site of N-methyl-D-aspartate receptors. *Mol. Pharmacol.* 84:114–127. https://doi.org/10.1124/mol.113.085803

Heyer, L.J., S. Kruglyak, and S. Yooseph. 1999. Exploring expression data: identification and analysis of coexpressed genes. *Genome Res.* 9:1106–1115. https://doi.org/10.1101/gr.9.11.1106

Humphrey, W., A. Dalke, and K. Schulten. 1996. VMD: visual molecular dynamics. *J. Mol. Graph.* 14:33–38: 27–28. https://doi.org/10.1016/0263-7855(96)00018-5

Iacobucci, G.J., and G.K. Popescu. 2017. Resident calmodulin primes NMDA receptors for Ca2+-dependent inactivation. *Biophys. J.* 113:2236–2248. https://doi.org/10.1016/j.bpj.2017.06.035

Inanobe, A., H. Furukawa, and E. Gouaux. 2005. Mechanism of partial agonist action at the NR1 subunit of NMDA receptors. *Neuron.* 47:71–84. https://doi.org/10.1016/j.neuron.2005.05.022

Jackson, M.B., B.S. Wong, C.E. Morris, H. Lecar, and C.N. Christian. 1983. Successive openings of the same acetylcholine receptor channel are correlated in open time. *Biophys. J.* 42:109–114. https://doi.org/10.1016/S0006-3495(83)84375-6

Jahr, C.E., and C.F. Stevens. 1993. Calcium permeability of the N-methyl-D-aspartate receptor channel in hippocampal neurons in culture. *Proc. Natl. Acad. Sci. USA.* 90:11573–11577. https://doi.org/10.1073/pnas.90.24.11573

Jalali-Yazdi, F., S. Chowdhury, C. Yoshioka, and E. Gouaux. 2018. Mechanisms for zinc and proton inhibition of the GluN1/GluN2A NMDA receptor. *Cell.* 175:1520–1532.e15. https://doi.org/10.1016/j.cell.2018.10.043

Jin, R., T.G. Banke, M.L. Mayer, S.F. Traynelis, and E. Gouaux. 2003. Structural basis for partial agonist action at ionotropic glutamate receptors. *Nat. Neurosci.* 6:803–810. https://doi.org/10.1038/nn1091

Karakas, E., and H. Furukawa. 2014. Crystal structure of a heterotetrameric NMDA receptor ion channel. *Science.* 344:992–997. https://doi.org/10.1126/science.1251915

Karakas, E., M.C. Regan, and H. Furukawa. 2015. Emerging structural insights into the function of ionotropic glutamate receptors. *Trends Biochem. Sci.* 40:328–337. https://doi.org/10.1016/j.tibs.2015.04.002

Krupp, J.J., B. Vissel, S.F. Heinemann, and G.L. Westbrook. 1998. N-terminal domains in the NR2 subunit control desensitization of NMDA receptors. *Neuron.* 20:317–327. https://doi.org/10.1016/S0896-6273(00)80459-6

Laskowski, R.A., J. Jabłońska, L. Pravda, R.S. Vařeková, and J.M. Thornton. 2018. PDBsum: Structural summaries of PDB entries. *Protein Sci.* 27:129–134. https://doi.org/10.1002/pro.3289

Lee, C.H., W. Lü, J.C. Michel, A. Goehring, J. Du, X. Song, and E. Gouaux. 2014. NMDA receptor structures reveal subunit arrangement and pore architecture. *Nature.* 511:191–197. https://doi.org/10.1038/nature13548

Lemke, J.R., R. Hendrickx, K. Geider, B. Laube, M. Schwake, R.J. Harvey, V.M. James, A. Pepler, I. Steiner, K. Hörtnagel, et al. 2014. GRIN2B mutations in West syndrome and intellectual disability with focal epilepsy. *Ann. Neurol.* 75:147–154. https://doi.org/10.1002/ana.24073

Lemke, J.R., K. Geider, K.L. Helbig, H.O. Heyne, H. Schütz, J. Hentschel, C. Courage, C. Depienne, C. Nava, D. Heron, et al. 2016. Delineating the GRIN1 phenotypic spectrum: A distinct genetic NMDA receptor encephalopathy. *Neurology.* 86:2171–2178. https://doi.org/10.1212/WNL.0000000000002740

Lester, R.A., J.D. Clements, G.L. Westbrook, and C.E. Jahr. 1990. Channel kinetics determine the time course of NMDA receptor-mediated synaptic currents. *Nature.* 346:565–567. https://doi.org/10.1038/346565a0

Liu, L., T.P. Wong, M.F. Pozza, K. Lingenhoehl, Y. Wang, M. Sheng, Y.P. Auberson, and Y.T. Wang. 2004. Role of NMDA receptor subtypes in governing the direction of hippocampal synaptic plasticity. *Science.* 304:1021–1024. https://doi.org/10.1126/science.1096615

Lomize, M.A., I.D. Pogozheva, H. Joo, H.I. Mosberg, and A.L. Lomize. 2012. OPM database and PPM web server: resources for positioning of proteins in membranes. *Nucleic Acids Res.* 40(D1):D370–D376. https://doi.org/10.1093/nar/gkr703

MacLean, D.M., R.J. Durham, and V. Jayaraman. 2019. Mapping the conformational landscape of glutamate receptors using single molecule FRET. *Trends Neurosci.* 42:128–139. https://doi.org/10.1016/j.tins.2018.10.003

Magleby, K.L., and B.S. Pallotta. 1983. Burst kinetics of single calcium-activated potassium channels in cultured rat muscle. *J. Physiol.* 344:605–623. https://doi.org/10.1113/jphysiol.1983.sp014958

Mayer, M.L. 2011. Emerging models of glutamate receptor ion channel structure and function. *Structure.* 19:1370–1380. https://doi.org/10.1016/j.str.2011.08.009

Monyer, H., R. Sprengel, R. Schoepfer, A. Herb, M. Higuchi, H. Lomeli, N. Burnashev, B. Sakmann, and P.H. Seeburg. 1992. Heteromeric NMDA receptors: molecular and functional distinction of subtypes. *Science.* 256:1217–1221. https://doi.org/10.1126/science.256.5060.1217

Ogden, K.K., and S.F. Traynelis. 2013. Contribution of the M1 transmembrane helix and pre-M1 region to positive allosteric modulation and gating of N-methyl-D-aspartate receptors. *Mol. Pharmacol.* 83:1045–1056. https://doi.org/10.1124/mol.113.085209

Ogden, K.K., W. Chen, S.A. Swanger, M.J. McDaniel, L.Z. Fan, C. Hu, A. Tankovic, H. Kusumoto, G.J. Kosobucki, A.J. Schulien, et al. 2017. Molecular mechanism of disease-associated mutations in the pre-M1 helix of NMDA receptors and potential rescue pharmacology. *PLoS Genet.* 13:e1006536. https://doi.org/10.1371/journal.pgen.1006536

Olney, J.W., J.W. Newcomer, and N.B. Farber. 1999. NMDA receptor hypofunction model of schizophrenia. *J. Psychiatr. Res.* 33:523–533. https://doi.org/10.1016/S0022-3956(99)00029-1

Paoletti, P., C. Bellone, and Q. Zhou. 2013. NMDA receptor subunit diversity: impact on receptor properties, synaptic plasticity and disease. *Nat. Rev. Neurosci.* 14:383–400. https://doi.org/10.1038/nrn3504

Piovesan, D., G. Minervini, and S.C.E. Tosatto. 2016. The RING 2.0 web server for high quality residue interaction networks. *Nucleic Acids Res.* 44(W1):W367-W374. https://doi.org/10.1093/nar/gkw315

Popescu, G., and A. Auerbach. 2004. The NMDA receptor gating machine: lessons from single channels. *Neuroscientist.* 10:192–198. https://doi.org/10.1177/1073858404263483

Popescu, G., A. Robert, J.R. Howe, and A. Auerbach. 2004. Reaction mechanism determines NMDA receptor response to repetitive stimulation. *Nature.* 430:790–793. https://doi.org/10.1038/nature02775

Qin, F., A. Auerbach, and F. Sachs. 1996. Estimating single-channel kinetic parameters from idealized patch-clamp data containing missed events. *Biophys. J.* 70:264–280. https://doi.org/10.1016/S0006-3495(96)79568-1

Qin, F., A. Auerbach, and F. Sachs. 1997. Maximum likelihood estimation of aggregated Markov processes. *Proc. Biol. Sci.* 264:375–383. https://doi.org/10.1098/rspb.1997.0054

Ren, H., A.K. Salous, J.M. Paul, R.H. Lipsky, and R.W. Peoples. 2007. Mutations at F637 in the NMDA receptor NR2A subunit M3 domain influence agonist potency, ion channel gating and alcohol action. *Br. J. Pharmacol.* 151:749–757. https://doi.org/10.1038/sj.bjp.0707254

Rice, A.C., and R.J. DeLorenzo. 1998. NMDA receptor activation during status epilepticus is required for the development of epilepsy. *Brain Res.* 782:240–247. https://doi.org/10.1016/S0006-8993(97)01285-7

Rycroft, B.K., and A.J. Gibb. 2002. Direct effects of calmodulin on NMDA receptor single-channel gating in rat hippocampal granule cells. *J. Neurosci.* 22:8860–8868. https://doi.org/10.1523/JNEUROSCI.22-20-08860.2002

Sali, A., and T.L. Blundell. 1993. Comparative protein modelling by satisfaction of spatial restraints. *J. Mol. Biol.* 234:779–815. https://doi.org/10.1006/jmbi.1993.1626

Schorge, S., S. Elenes, and D. Colquhoun. 2005. Maximum likelihood fitting of single channel NMDA activity with a mechanism composed of independent dimers of subunits. *J. Physiol.* 569:395–418. https://doi.org/10.1113/jphysiol.2005.095349

Sobolevsky, A.I., C. Beck, and L.P. Wollmuth. 2002. Molecular rearrangements of the extracellular vestibule in NMDAR channels during gating. *Neuron.* 33:75–85. https://doi.org/10.1016/S0896-6273(01)00560-8

Sobolevsky, A.I., M.L. Prodromou, M.V. Yelshansky, and L.P. Wollmuth. 2007. Subunit-specific contribution of pore-forming domains to NMDA receptor channel structure and gating. *J. Gen. Physiol.* 129:509–525. https://doi.org/10.1085/jgp.200609718

Sobolevsky, A.I., M.P. Rosconi, and E. Gouaux. 2009. X-ray structure, symmetry and mechanism of an AMPA-subtype glutamate receptor. *Nature.* 462:745–756. https://doi.org/10.1038/nature08624

Sun, Y., R. Olson, M. Horning, N. Armstrong, M. Mayer, and E. Gouaux. 2002. Mechanism of glutamate receptor desensitization. *Nature.* 417:245–253. https://doi.org/10.1038/417245a

Swanger, S.A., W. Chen, G. Wells, P.B. Burger, A. Tankovic, S. Bhattacharya, K.L. Strong, C. Hu, H. Kusumoto, J. Zhang, et al. 2016. Mechanistic insight into NMDA receptor dysregulation by rare variants in the GluN2A and GluN2B agonist binding domains. *Am. J. Hum. Genet.* 99: 1261–1280. https://doi.org/10.1016/j.ajhg.2016.10.002

Tajima, N., E. Karakas, T. Grant, N. Simorowski, R. Diaz-Avalos, N. Grigorieff, and H. Furukawa. 2016. Activation of NMDA receptors and the mechanism of inhibition by ifenprodil. *Nature.* 534:63–68. https://doi.org/10.1038/nature17679

Talukder, I., and L.P. Wollmuth. 2011. Local constraints in either the GluN1 or GluN2 subunit equally impair NMDA receptor pore opening. *J. Gen. Physiol.* 138:179–194. https://doi.org/10.1085/jgp.201110623

Talukder, I., P. Borker, and L.P. Wollmuth. 2010. Specific sites within the ligand-binding domain and ion channel linkers modulate NMDA receptor gating. *J. Neurosci.* 30:11792–11804. https://doi.org/10.1523/JNEUROSCI.5382-09.2010

Traynelis, S.F., L.P. Wollmuth, C.J. McBain, F.S. Menniti, K.M. Vance, K.K. Ogden, K.B. Hansen, H. Yuan, S.J. Myers, and R. Dingledine. 2010. Glutamate receptor ion channels: structure, regulation, and function. *Pharmacol. Rev.* 62:405–496. https://doi.org/10.1124/pr.109.002451

Twomey, E.C., and A.I. Sobolevsky. 2018. Structural mechanisms of gating in ionotropic glutamate receptors. *Biochemistry.* 57:267–276. https://doi.org/10.1021/acs.biochem.7b00891

Twomey, E.C., M.V. Yelshanskaya, R.A. Grassucci, J. Frank, and A.I. Sobolevsky. 2017. Channel opening and gating mechanism in AMPA-subtype glutamate receptors. *Nature.* 549:60–65. https://doi.org/10.1038/nature23479

Vance, K.M., N. Simorowski, S.F. Traynelis, and H. Furukawa. 2011. Ligand-specific deactivation time course of GluN1/GluN2D NMDA receptors. *Nat. Commun.* 2:294. https://doi.org/10.1038/ncomms1295

Vance, K.M., K.B. Hansen, and S.F. Traynelis. 2012. GluN1 splice variant control of GluN1/GluN2D NMDA receptors. *J. Physiol.* 590:3857–3875. https://doi.org/10.1113/jphysiol.2012.234062

XiangWei, W., Y. Jiang, and H. Yuan. 2018. De novo mutations and rare variants occurring in NMDA receptors. *Curr. Opin. Physiol.* 2:27–35. https://doi.org/10.1016/j.cophys.2017.12.013

Yelshanskaya, M.V., A.K. Singh, J.M. Sampson, C. Narangoda, M. Kurnikova, and A.I. Sobolevsky. 2016. Structural bases of noncompetitive inhibition of AMPA-subtype ionotropic glutamate receptors by antiepileptic drugs. *Neuron.* 91:1305–1315. https://doi.org/10.1016/j.neuron.2016.08.012

Yuan, H., K. Erreger, S.M. Dravid, and S.F. Traynelis. 2005. Conserved structural and functional control of N-methyl-D-aspartate receptor gating by transmembrane domain M3. *J. Biol. Chem.* 280:29708–29716. https://doi.org/10.1074/jbc.M414215200

Yuan, H., S.J. Myers, G. Wells, K.L. Nicholson, S.A. Swanger, P. Lyuboslavsky, Y.A. Tahirovic, D.S. Menaldino, T. Ganesh, L.J. Wilson, et al. 2015. Context-dependent GluN2B-selective inhibitors of NMDA receptor function are neuroprotective with minimal side effects. *Neuron.* 85: 1305–1318. https://doi.org/10.1016/j.neuron.2015.02.008

Zhang, J.B., S. Chang, P. Xu, M. Miao, H. Wu, Y. Zhang, T. Zhang, H. Wang, J. Zhang, C. Xie, et al. 2018. Structural basis of the proton sensitivity of human GluN1-GluN2A NMDA receptors. *Cell Rep.* 25:3582–3590.e4. https://doi.org/10.1016/j.celrep.2018.11.071

Zhu, X., S. Petrovski, P. Xie, E.K. Ruzzo, Y.F. Lu, K.M. McSweeney, B. Ben-Zeev, A. Nissenkorn, Y. Anikster, D. Oz-Levi, et al. 2015. Whole-exome sequencing in undiagnosed genetic diseases: interpreting 119 trios. *Genet. Med.* 17:774–781. https://doi.org/10.1038/gim.2014.191

Supplemental material

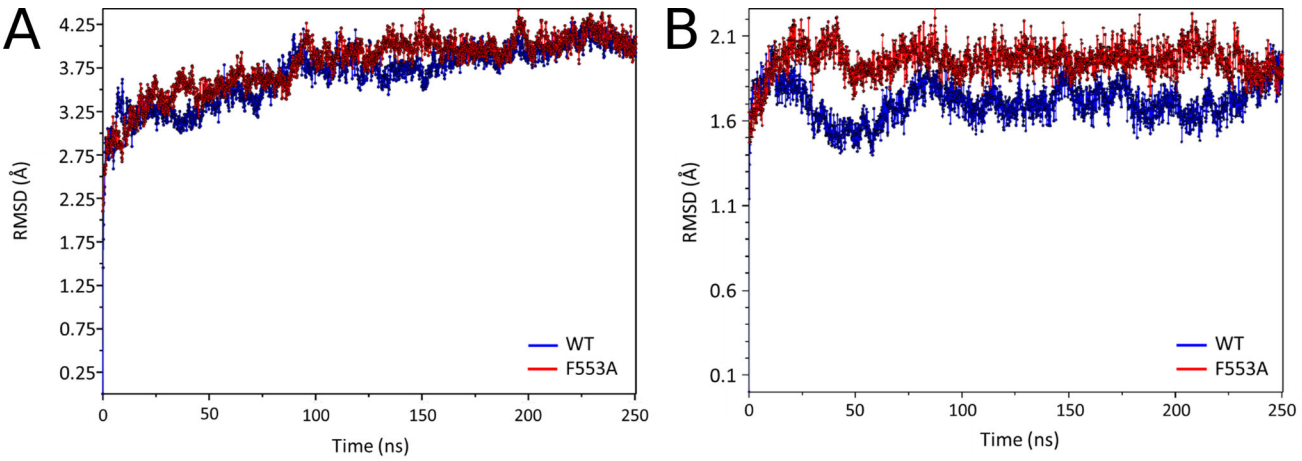

C

RMSD	Avg (Å)	SD (Å)	Min (Å)	Max (Å)
Alignments based on chains A-D or protein				
WT/F553A Protein (chains A-D)	**3.67/3.79**	**0.34/0.34**	**2.01/2.10**	**4.31/4.43**
WT/F553A Chain A	3.61/3.35	0.33/0.25	2.05/1.99	4.41/4.05
WT/F553A Chain B	3.59/3.57	0.70/0.33	1.89/1.83	4.92/4.28
WT/F553A Chain C	2.78/3.11	0.28/0.31	1.69/1.75	3.58/4.19
WT/F553A Chain D	3.60/3.83	0.26/0.45	1.97/2.06	4.35/4.78
Alignment based on M3 helices (Chain A/C residues 627-654 and chain B/D residues 623-653)				
WT/F553A Protein (Chains A-D)	**1.71/1.95**	**0.11/0.09**	**1.49/1.47**	**2.06/2.26**
WT/F553A Chain A	1.00/1.29	0.15/0.13	0.67/0.70	1.45/1.71
WT/F553A Chain B	1.56/1.68	0.13/0.10	1.34/1.33	2.09/2.03
WT/F553A Chain C	1.02/1.20	0.12/0.14	0.69/0.75	1.54/1.72
WT/F553A Chain D	1.37/1.13	0.18/0.13	0.67/0.65	2.35/1.55

Figure S1. **RMSD calculations are provided for each MD simulation (WT and F553A) based on two distinct alignments; RMSD values are calculated with the minimized model as the reference structure.** The first is an alignment of the entire protein (used in the simulation) and the second is an alignment on the M3 helices of the TMD alone (including all four M3 helices, chains A–D, in the alignment). **(A)** The backbone RMSD plots for each trajectory aligned on the entire protein over the 250-ns simulation are shown. Blue represents WT GluN2A and red represents GluN2A-F553A. **(B)** The backbone RMSD is plotted for the individual M3 helices, with the trajectory aligned on the M3 helices. Blue represents WT GluN2A and red represents GluN2A-F553A. **(C)** A statistical analysis of the RMSD calculations is provided for each simulation (WT and F553A) based on the two distinct alignments. For each alignment, if the RMSD column states "WT/F553A Protein," it represents the RMSD values calculated using chains A–D of the WT and F553A. Similarly, if the RMSD column states "WT/F553A chain A, B, C, or D," it represents the RMSD value calculated for that specific chain given a particular alignment. Frame 1 was used as the reference frame in all RMSD calculations.

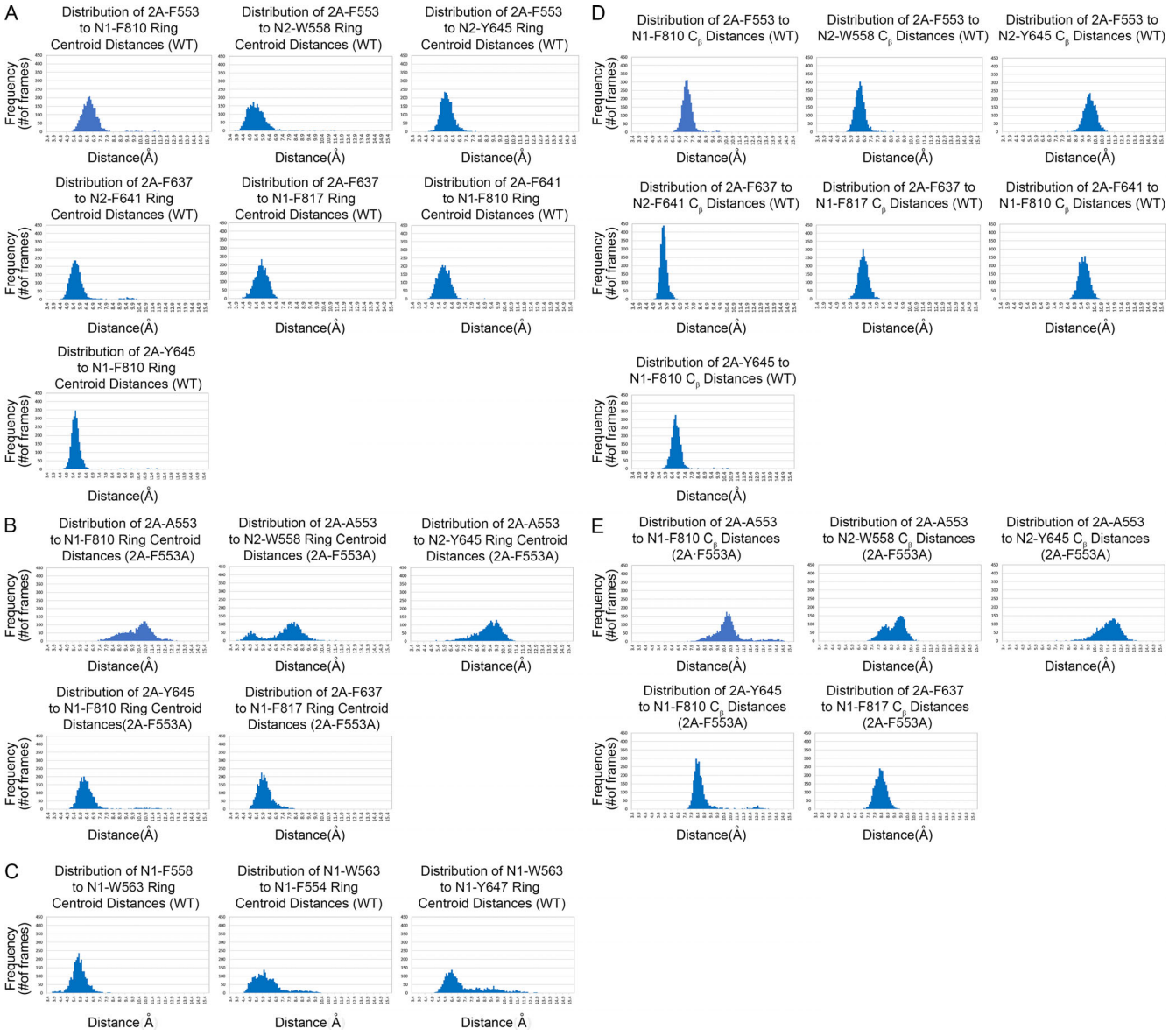

Figure S2. **Distribution plots for distances between the residues shown in Fig. 6. (A)** WT simulation, GluN2A subunit, and ring centroid distances. **(B)** GluN1/GluN2A-F553A simulation, GluN2A subunit, and ring centroid distances. **(C)** WT simulation, GluN1 subunit, and ring centroid distances. **(D)** C_β distances for the pairs of residues represented in A. **(E)** C_β distances for the pairs of residues represented in B.

A

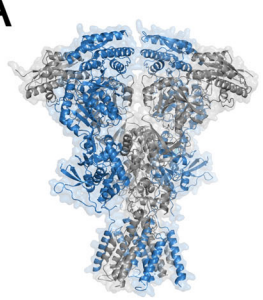

SeqID/ SeqSim	Q05586*	GluN1#	5FXH	4PE5	5L1B
Q05586*	100/100				
GluN1#	95.5/95.5	100/100			
5FXH	90.3/91.5	94.5/95.8	100/100		
4PE5	88/89.2	92.2/93.4	95.8/96.1	100/100	
5L1B	5.4/10.1	5.6/10.6	5.5/10.2	5/8.9	100/100

Note: The sequence identity and similarity of the TM region between GluN1 and 5L1B is 30.2/57
*__Q05586__ represent the full length sequence for GluN1 and is the unique Uniprot entry identification
#__GluN1__ is the actual portion of the the sequence used for model generation

B

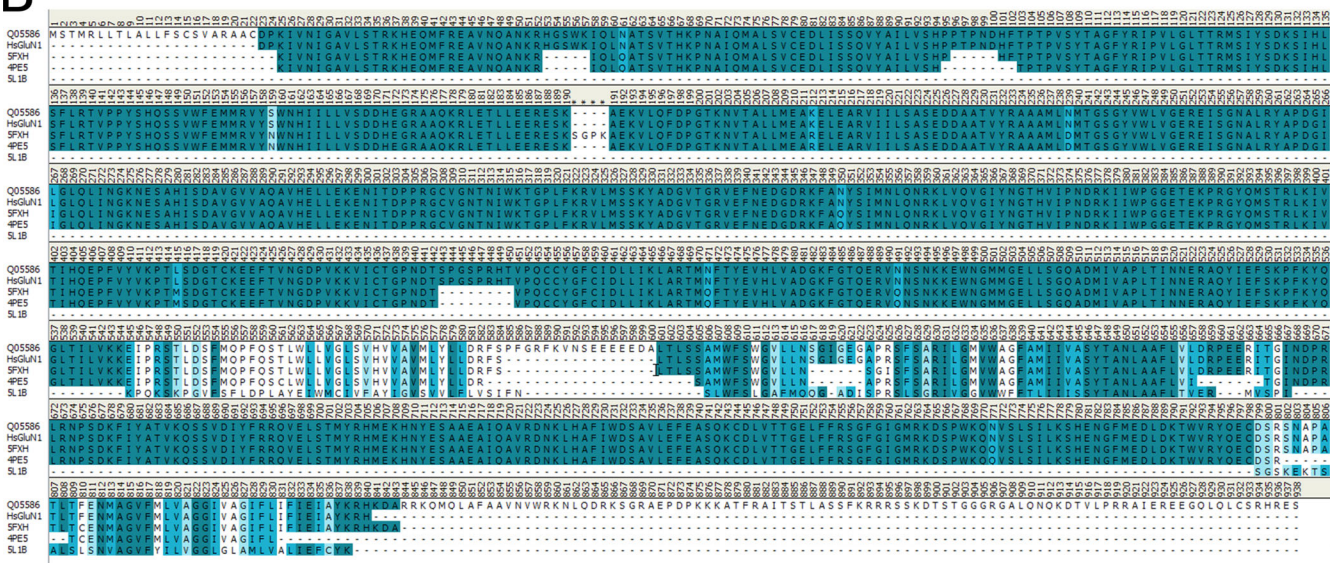

Figure S3. **Sequence alignments used for homology model building. (A)** An image of a full-length di-heterotetramer GluN1 (gray)/GluN2A (blue) NMDA structure. The table provides the sequence identity (SeqID) and sequence similarity (SeqSim) of the template and target sequences used for GluN1. **(B)** The sequence alignment used for GluN1 during model building.

A

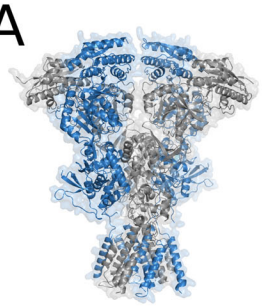

SeqID/ SeqSim	Q128792*	GluN2A#	5FXH	4PE5	5L1B
Q128792*	**100/100**				
GluN2A#	94.4/94.3	**100/100**			
5FXH	65.1/79.2	69.1/84.0	**100/100**		
4PE5	60.4/74.3	64.0/78.7	92.6/92.7	**100/100**	
5L1B	4.7/9.8	5.0/10.4	4.9/9.6	4.1/7.4	**100/100**

Note: The sequence identity and similarity of the TM region between GluN2A and 5L1B is 27.6/57.2
*__Q128782__ represent the full length sequence for GluN2A and is the unique Uniprot entry identification
#__GluN2A__ is the actual portion of the the sequence used for model generation

B

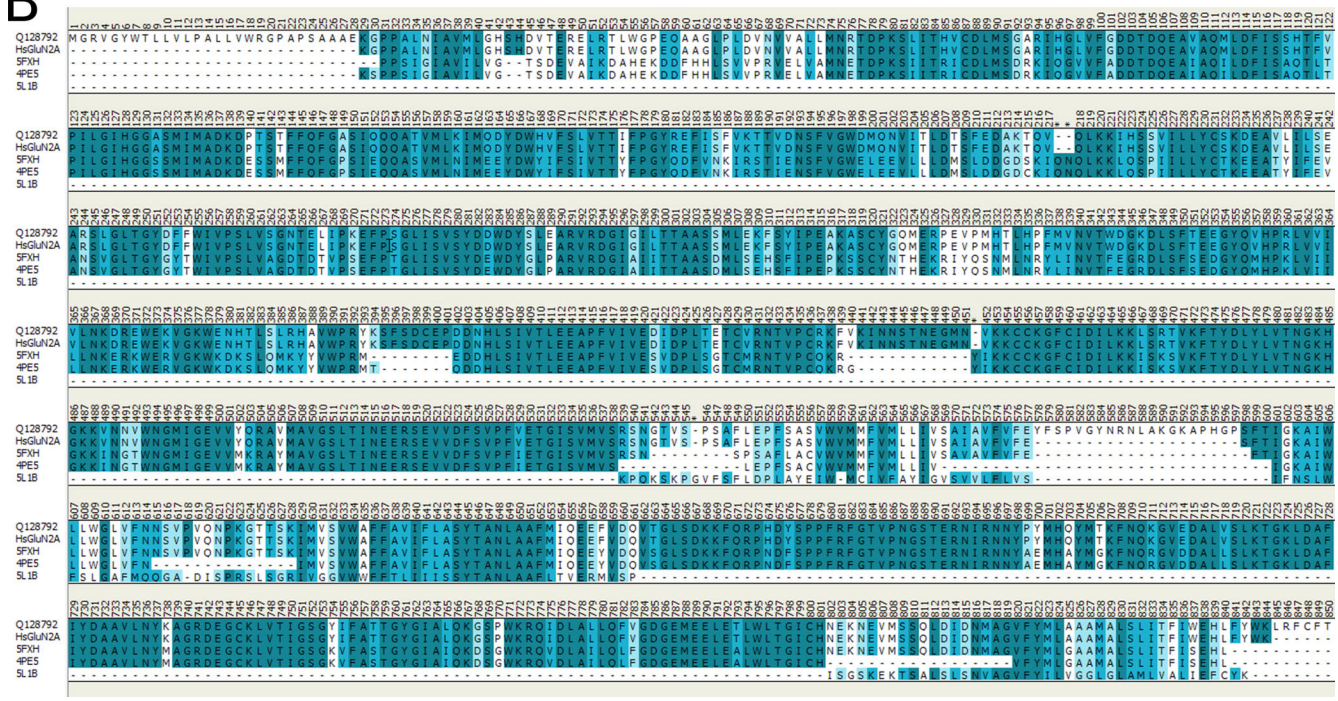

Figure S4. **Sequence alignments used for homology model building. (A)** An image of a full-length di-heterotetramer GluN1 (gray)/GluN2A (blue) NMDA structure. The table provides the sequence identity (SeqID) and sequence similarity (SeqSim) of the template and target sequences used for GluN2. **(B)** The sequence alignment used for GluN2A during model building. The amino acids at the amino terminal with no template are not shown.

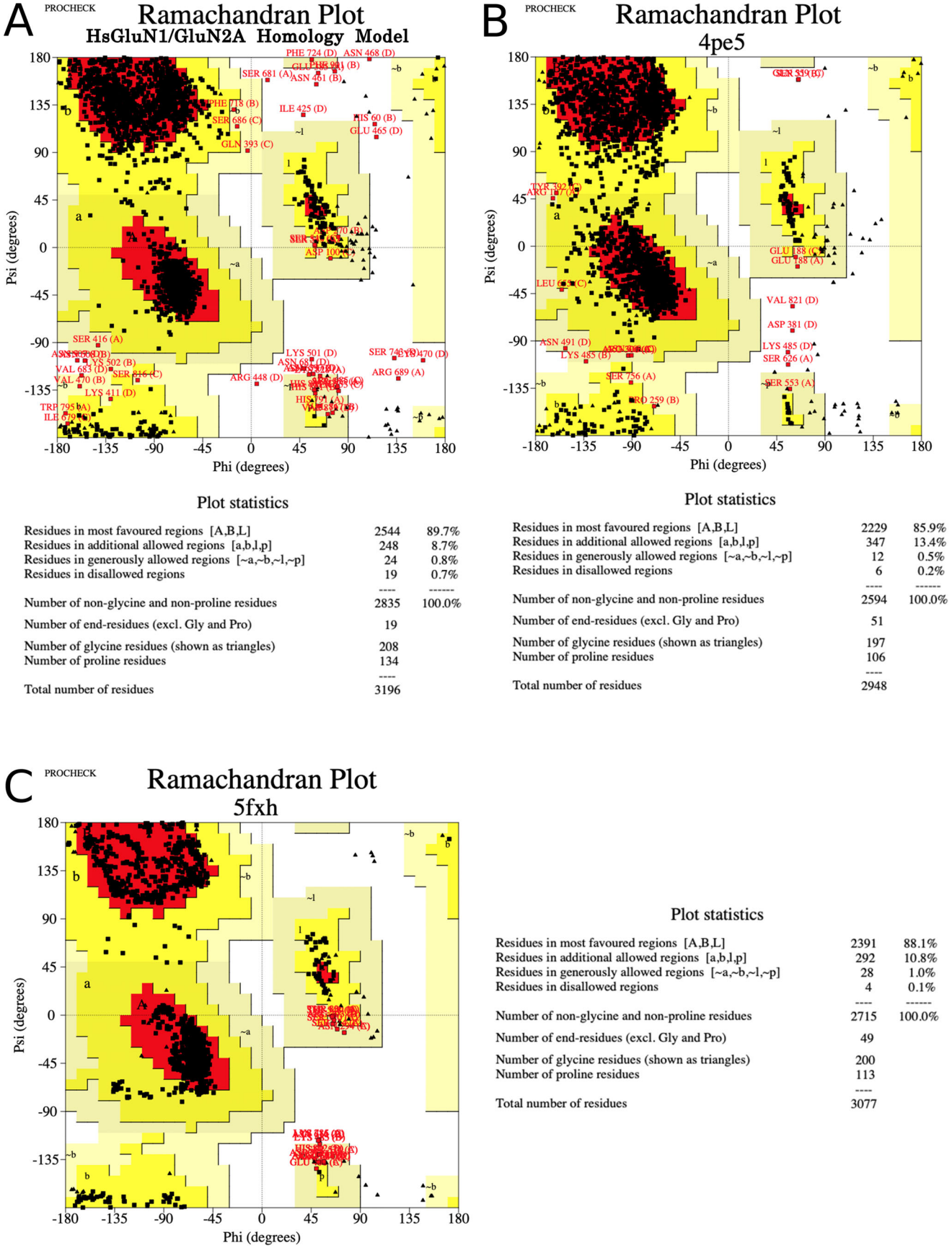

Plot statistics

Residues in most favoured regions [A,B,L]	2544	89.7%
Residues in additional allowed regions [a,b,l,p]	248	8.7%
Residues in generously allowed regions [~a,~b,~l,~p]	24	0.8%
Residues in disallowed regions	19	0.7%
Number of non-glycine and non-proline residues	2835	100.0%
Number of end-residues (excl. Gly and Pro)	19	
Number of glycine residues (shown as triangles)	208	
Number of proline residues	134	
Total number of residues	3196	

Plot statistics

Residues in most favoured regions [A,B,L]	2229	85.9%
Residues in additional allowed regions [a,b,l,p]	347	13.4%
Residues in generously allowed regions [~a,~b,~l,~p]	12	0.5%
Residues in disallowed regions	6	0.2%
Number of non-glycine and non-proline residues	2594	100.0%
Number of end-residues (excl. Gly and Pro)	51	
Number of glycine residues (shown as triangles)	197	
Number of proline residues	106	
Total number of residues	2948	

Plot statistics

Residues in most favoured regions [A,B,L]	2391	88.1%
Residues in additional allowed regions [a,b,l,p]	292	10.8%
Residues in generously allowed regions [~a,~b,~l,~p]	28	1.0%
Residues in disallowed regions	4	0.1%
Number of non-glycine and non-proline residues	2715	100.0%
Number of end-residues (excl. Gly and Pro)	49	
Number of glycine residues (shown as triangles)	200	
Number of proline residues	113	
Total number of residues	3077	

Figure S5. **Ramachandran plots. (A)** The di-heteromeric GluN1a/GluN2A homology model selected for this study. **(B)** The di-heteromeric template used PDB identifier 4PE5 (GluN1/GluN2B). **(C)** The second di-heteromeric template used PDB identifier 5FXH (GluN1/GluN2B) consisting of only backbone atoms.

A

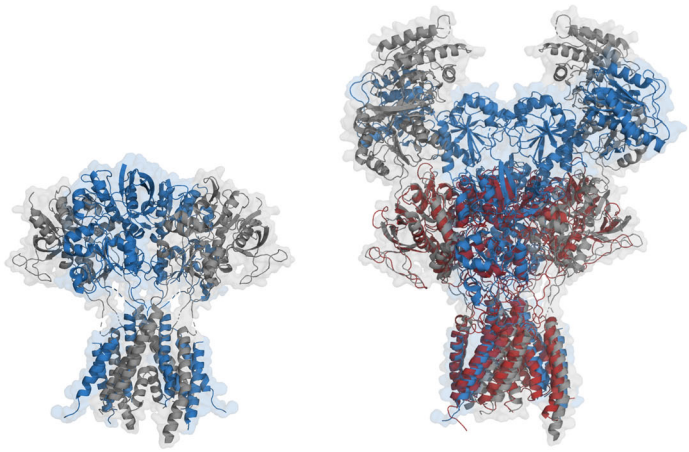

B

SeqID/ SeqSim	Q05586*	GluN1#	5FXH	4PE5	5L1B
Q05586*	**100/100**				
GluN1#	96.4/96.4	**100/100**			
5FXH	91.5/92.7	94.9/96.0	**100/100**		
4PE5	86.9/88.1	90.2/91.4	93.8/94.3	**100/100**	
5L1B	10.1/19.1	10.5/19.8	10.2/19.0	9.4/16.7	**100/100**

Note: The sequence identity and similarity of the TM region between GluN1 and 5L1B is 30.2/57
*__Q05586__ represents the full length sequence for GluN1 and is the unique Uniprot entry identification
#__GluN1__ is the actual portion of the the sequence used for model generation

C

SeqID/ SeqSim	Q128792*	GluN2A#	5FXH	4PE5	5L1B
Q128792*	**100/100**				
GluN2A#	95.3/95.3	**100/100**			
5FXH	78.4/95.3	83.2/88.8	**100/100**		
4PE5	68.6/86.6	72.1/78.3	86.4/86.4	**100/100**	
5L1B	9.5/19.6	9.8/20.6	9.9/19.0	8.3/14.7	**100/100**

Note: The sequence identity and similarity of the TM region between GluN2A and 5L1B is 27.6/57.2
*__Q128782__ represent the full length sequence for GluN2A and is the unique Uniprot entry identification
#__GluN2A__ is the actual portion of the the sequence used for model generation

Figure S6. **Overlay of the model used for MD simulations with a recently published cryo-EM structure of a GluN1/GluN2A receptor. (A)** Left: An image of a di-heterotetramer GluN1 (gray)/GluN2A (blue) NMDA structure without the ATD. Right: An overlay of the GluN1a/GluN2A model (red) and a GluN1/GluN2A cryo-EM structure (PDB identifier, 6IRA; resolution, 4.5 Å). **(B and C)** The tables provide the sequence identity (SeqID) and sequence similarity (SeqSim) of the template and target sequences used for GluN1 (B) and GluN2A (C).

Table S1 is provided online as a separate Word file and lists the models used in the MD simulations.